

Rijksuniversiteit Groningen
Zernike Institute of Advanced Materials
Nanostructured Materials and Interfaces

Reversible phase transformations in SeTe(As/Sb) combining ultrafast DSC and electron microscopy

7 December 2016

Author

Joost Calon
s2166593

Supervisor

prof. dr. ir. Bart Kooi

Second supervisor

prof. dr. George Palasantzas

Daily supervisor

Paul Vermeulen

Abstract

The reversible crystalline-amorphous transition of SeTeAs/SeTeSb has been investigated by the use of ultrafast DSC by using heating rates of 1 to 10^4 K/s. In the SeTeSb sample, Se_3Sb_2 crystals were formed which limited the influence of the antimony compared to SeTe. Furthermore, it was possible to switch SeTeAs reversibly between the crystalline and amorphous phase. SeTeAs was found to be a better glass former than SeTe, the critical quench rate of SeTeAs was found to be a factor 100 times lower than SeTe. At low temperatures, new transitions started showing up below 220 °C which decreased the heat capacity during crystallization and increased the heat capacity in another transition occurring at 250 – 300 °C. Isothermal measurements at 140 – 160 °C also showed a transition around 200 – 220 °C when the sample was reheated. Because ultrafast DSC did not provide a full explanation for the transitions occurring, a new method has been successfully developed to transfer samples treated in a Flash DSC to a scanning (SEM) or transmission electron microscope (TEM). By the use of this method the structure of SeTe was investigated with a TEM which was fully crystalline with crystals in the size order of 0.1 to 1 μm . Furthermore, heat treated samples of $\text{Se}_{45}\text{Te}_{45}\text{As}_{10}$ that were crystallized at 5, 100 and -100 K/s were investigated with a TEM. These samples had a spherulitic structure which contained crystal lamella in the size order of 100 nm which was surrounded by amorphous material. Both SeTe and SeTeAs were measured to have a crystal structure belonging to the trigonal lattice system and had a $P\ 3_1\ 2\ 1$ symmetry. By the use of electron diffraction on SeTeAs, the lamella are found to grow in the $\{-1\ 2\ 0\}$ or $\{-1\ 3\ 0\}$ direction. Furthermore, Energy-Dispersive X-ray Spectroscopy (EDS) and Scanning Transmission Electron Microscopy (STEM) were used to investigate the composition of SeTeAs. It was found that the arsenic segregated into the amorphous phase (15 - 20 at%). Also, the amorphous phase contained 10 to 50 at% more selenium and 20 – 50 at% less tellurium than the crystal phase. The heating rates of 5 and 100 K/s did not seem to have a large influence on the composition and structure.

Table of contents

1. Introduction	2
2. Theory	3
2.1 Phase change materials	3
2.2 Structure and properties of SeTe(M) alloys	6
3. Experimental	7
3.1 Basics of (ultrafast) DSC	7
3.2 Making samples and performing experiments with Flash DSC	8
3.3 Microscopy	12
3.4 Sample preparation: from Flash DSC to electron microscope	13
4. Results and discussion	17
4.1 Structure of (heat treated) SeTe	17
4.2 Thermal properties measured by DSC of SeTeAs	20
4.2.1 Heating rates and composition	21
4.2.2 Kissinger analysis	25
4.2.3 Isothermal measurements	28
4.2.4 Discussion	30
4.3 Structure and thermal properties measured by DSC of SeTeSb	30
4.4 Structure of (heat treated) SeTeAs	34
4.4.1 Microstructure overview	36
4.4.2 Nanostructure overview	39
4.4.3 Composition	42
4.4.4 Atomic structure	46
4.4.5 Discussion	50
5. Conclusions	51
6. Outlook	52
7. Acknowledgements	52
8. References	53
Appendix A: Phase diagrams	55
Appendix B: Crystallinity and crystal size calculations	56
Appendix C: Structure factor of the trigonal system and $P\bar{3}_121$ space group	57
Appendix D: Composition data of SeTeAs	58

1. Introduction

Phase-change materials (PCMs) are materials that can change their structure on the atomic scale when applying heat, light or electrical current^{1,2}. This can be for example (re)crystallization, reorganization or phase segregation. The difference in properties between the initial and final phases can be exploited and PCMs are used in a variety of applications like data storage³⁻⁶ and energy storage⁷⁻¹⁰. For example, in data storage the difference in resistance or optical contrast between the amorphous and crystalline states is used to store information in the material¹¹. Furthermore, a general understanding of phase transitions is also useful for the production of materials since these often involve phase changes to obtain the right structure and properties for the final material. This particularly holds for the complex phase transformations occurring in many steel grades^{12,13}.

An important tool to characterize phase changes is Differential Scanning Calorimetry (DSC) which allows the heat flow of a material to be measured while the temperature is changed as variable. This makes it possible to measure transitions like the glass transitions, (re)crystallization and melting of a material. While a conventional DSC is able to heat a sample with heating rates up to 1 K/s, ultrafast DSC allows heating and cooling rates up to 10^4 K/s¹⁴. This increases the possibilities to measure the amorphous/crystalline phase change in phase change memories directly^{15,16} as well as measuring the crystal growth properties to investigate growth theories^{17,18}.

A disadvantage of the DSC is that even though it gives much thermal information about the phase transitions happening in a material, it does not provide details about how the structure changes. For normal DSC, the samples are in the order of mg in weight which makes it relatively easy to produce samples for microscopy or other measuring techniques. However, ultrafast DSC requires much smaller samples which weigh below the μg and sizes in the order of 10 – 100 μm which makes sample preparation difficult. The structural changes of phase-change materials have been previously investigated by Transmission Electron Microscopy (TEM) with the use of electric pulses¹⁹. One problem of this is that the temperature is not directly controlled and not known during the phase transition. Also it does not provide important details about the phase transformation such as transition temperatures, crystallization energies and heat capacity.

The aim of this research is to switch alloys reversibly between the amorphous and crystalline phase by the use of ultrafast DSC to investigate thermal properties such as the glass transition, crystallization and melting temperature (and to a lesser extend the crystallization and melting enthalpies and heat capacity). Because ultrafast DSC is currently limited by its heating rate and maximum temperature, it is not possible to use it to investigate commonly used phase change materials such as $\text{Ge}_2\text{Sb}_2\text{Se}_5$ (GST). Previous research has thus focussed on the thermal properties of SeTe alloys²⁰ which can be switched reversibly with the use of ultrafast DSC. This research extends on this previous research by investigating the mentioned thermal properties of the ternary alloys SeTeAs and SeTeSb. Furthermore, a method is developed to couple the Flash DSC to Scanning Electron Microscopy (SEM) and TEM by removing the sample from the Flash DSC sensor and treating it to do ex-situ SEM and TEM analysis. By using this method, the structural properties of SeTeAs can be directly coupled and correlated to various thermal treatments performed in the Flash DSC.

2. Theory

2.1 Phase change materials

Phase-change materials are materials that are able to switch rapidly and reversibly between a crystalline structure and an amorphous structure and they offer large property (e.g. optical, electrical) contrast between the two phases which makes them highly suited for memory applications²¹. The switching between the two phases can generally be done by applying a light pulse, an electrical current (pulse) or by heating the material. In this research, the last one will be used. To get the material into the amorphous state, it has to be brought to the melt where the atoms have large mobility and do not form ordered structures (although still short-range order can be present). Then, when the material is cooled quickly enough the atoms do not have enough time to crystallize in a regular lattice and are frozen at their position (Figure 1). Even though the Gibbs-free energy for the crystalline state is more favourable, at low energies the mobility of the atoms is too small to overcome the potential barrier to form a crystal. An amorphous material is hard and brittle at low temperatures, however at higher temperatures the mobility of the atoms starts increasing and the material becomes molten or rubber-like. The point at which this occurs is called the glass transition and it is defined at the point where the material has a viscosity of 10^{12} Pa s.

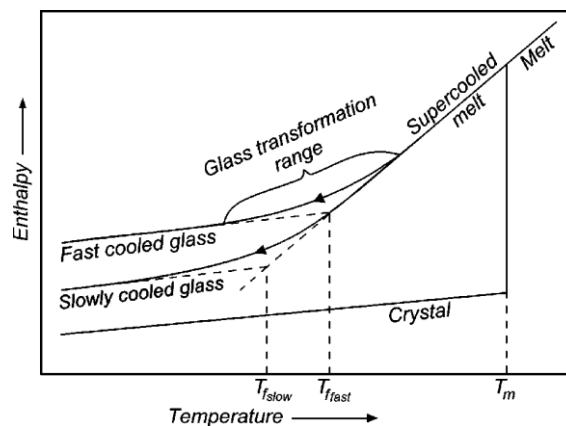


Figure 1: The enthalpy or volume of a material plotted against the temperature. When a material is slowly cooled from the melt crystallization occurs below T_m . When the material is cooled fast enough the material a glass is formed.²¹

The dynamics of a material in an undercooled liquid can be described by the viscosity. The viscosity is dependent on the temperature and the logarithm of the viscosity is often plotted against T_g/T which is called an Angell plot (Figure 2). By definition the viscosity at $T_g/T = 0$ is -2 while at $T_g/T = 1$ it is 12. When a material follows the Arrhenius equation it has a linear relation in the Angell plot and it is called a strong liquid. Opposed to this is a fragile liquid for which the viscosity increases less at a lower T_g/T while it increases more at a higher T_g/T ²².

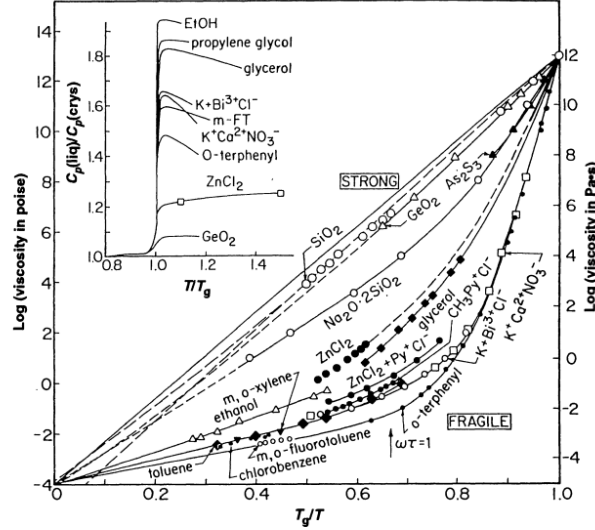


Figure 2: Angell plot which shows the logarithm of the viscosity as function of T_g/T for different materials. Strong liquids have a linear relationship in this graph while for fragile liquids the viscosity increases less at a lower T_g/T and more at a higher T_g/T .²³

Crystallization can occur by heating the amorphous state to above the glass transition temperature (and below melting temperature) or cooling slowly from the liquid state. Either way, the crystallization process can be described by two processes: nucleation and growth. The Gibbs-free energy for nucleation depends on the surface energy which has a radius (r) to the power 2 contribution and the difference in Gibbs-free energy for the amorphous and the crystalline state which has an r^3 contribution. Because of this there is a critical nucleus size below which the contribution of the surface energy is too large to grow and above which the nucleus will grow. The rate at which a process occurs can in general be described with the Arrhenius equation²⁴:

$$k = A \exp(E_a/k_b T) \quad (1)$$

where k is the reaction rate, A is a constant, E_a is the activation energy per atom k_b is the Boltzmann constant and T is the temperature. The activation energy can be obtained by finding the maximal reaction rate with respect to the time. This relation has been derived by Kissinger to obtain the relation between the activation energy, peak temperature (T_p) at which the reaction rate is highest and heating rate ϕ :

$$\ln\left(\frac{\Phi}{T_p^2}\right) = \ln\left(\frac{Ak_b}{E_a}\right) - \frac{E_a}{k_b T_p} \quad (2)$$

Thus the activation energy can be calculated by the slope of $\ln(\Phi/T_p^2)$ and $1/T_p$:

$$E_a = \frac{\partial(\ln(\Phi/T_p^2))}{\partial(1/T_p)} \quad (3)$$

In the case of crystal growth the peak temperature is called the crystallization temperature. It must be emphasised Formula 3 assumes that the growth rate is dependent on the temperature by the Arrhenius equation which is not always the case. For higher heating rates the crystallization temperature increases because crystallization is a thermally activated process. Faster heating will give the material less time to nucleate and grow which will therefore increase the crystallization temperature.

A time temperature transition diagram, as shown in Figure 3, shows an overview of the time and temperature conditions that are required to vitrify or crystallize a material. By changing the heating rate the crystallization region can be measured as shown by the set/reset pulses. However, another useful and more direct method to measure this region is by the use of isothermal measurements where the material is kept at a constant temperature for a certain time. By varying the time and temperature the whole crystallization region can then be probed.

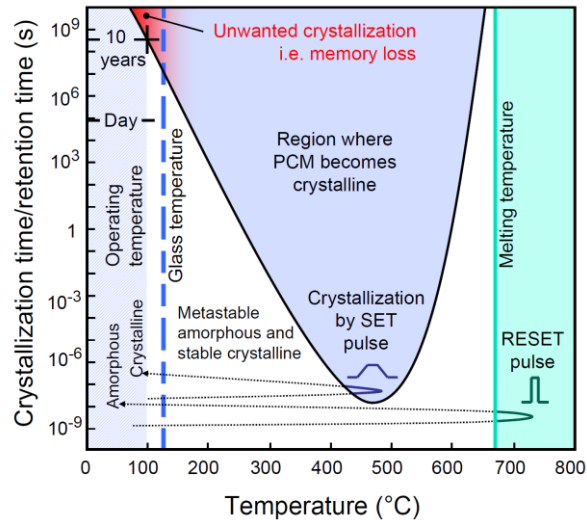


Figure 3: The time temperature transition diagram for crystallization of a phase change material. The diagram shows the glass transition, melting point and the region where the material becomes crystalline. With a set pulse the material can be crystallized in this region and with a reset pulse up to the melting point that is fast enough the material can be vitrified.²⁵

When the crystal is growing at a constant temperature, the crystallinity can be expressed as a function of time. According to the Johnson-Mehl-Avrami-Kolmogorov (JMAK) theory this will have the shape of an S-curve:

$$f(x) = 1 - \exp(-\beta \cdot t^k) \quad (4)$$

The parameter k is theoretically temperature independent and depends on two factors: the probability of formation of growth nuclei per germ nucleus per unit time n and the dimensionality of the growth²⁶⁻²⁸. This dependency is depicted in Table 1 which shows how the value k varies with these two.

	n large	n intermediate	n small
Lineal growth (one dimensional growth)	1	1 – 2	2
Plate-like growth (two dimensional)	2	2 – 3	3
Polyhedral growth (three dimensional)	3	3 – 4	4

Table 1: Values of the k parameter for different types of dimensional growth and different values for the probability of formation of growth nuclei per germ nucleus per unit time n.

As can be seen, the dimensionality adds one to two to the value of k and the probability n adds zero to one which will cause k to lie between one and four. The parameter β is dependent on the dimensionality of growth, growth rate, germ nuclei per volume and the probability of growth nuclei per germ nucleus per time unit.

2.2 Structure and properties of SeTe(M) alloys

$\text{Se}_{1-x}\text{Te}_x$ can be considered a phase-change material that has been previously investigated using ultrafast DSC²⁰. In the present research the ternary alloys SeTe(M) with M = Sb, As are investigated to study the influence of adding As and Sb on thermal behaviour and structure of the alloy. The melting temperatures of Se, Te, As and Sb are 221 °C, 450 °C, 817 °C and 631 °C, respectively, and their binary phase diagrams can be found in Appendix A. The cooling rates required to quench Se and Te to make them amorphous (critical quench rate) are 1 K/s and 10^{10} K/s, respectively. Earlier research showed that the critical quench rate of SeTe varies from 10 to 10^4 K/s for compositions with a Te percentage of 15 to 65 at%²⁰. The most common structure for both Se and Te is the trigonal structure with the P $3_1 2 1$ space group. This structure consists of long chains which have a threefold rotation symmetry as shown in Figure 4. The lattice parameters of selenium are $a = 4.368 \text{ \AA}$ and $c = 4.958 \text{ \AA}$ and for tellurium they are $a = 4.451 \text{ \AA}$ and $c = 5.926 \text{ \AA}$ ²⁹. Similar to selenium and tellurium, the most common crystalline structures of arsenic and antimony are also trigonal. The lattice parameters of arsenic are $a = 3.7598 \text{ \AA}$ and $c = 10.5475 \text{ \AA}$ ³⁰ and for antimony they are $a = 4.3084 \text{ \AA}$ and $c = 11.274 \text{ \AA}$ ³¹.

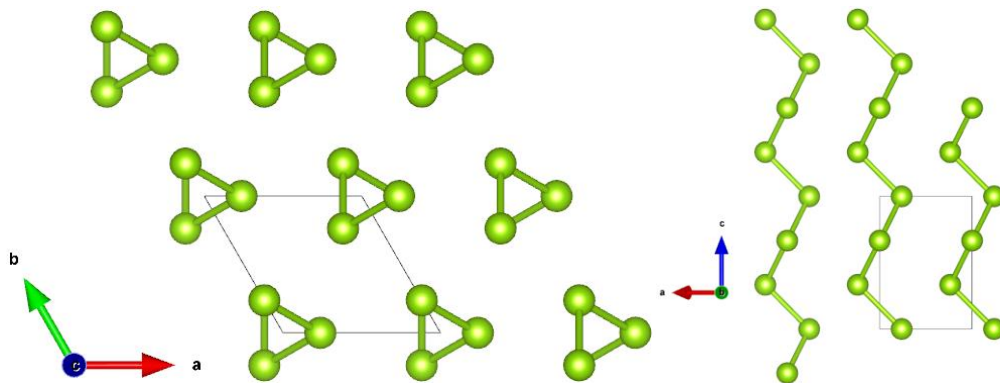


Figure 4: The most common structure of selenium and tellurium along the c axis (left) and along the b axis (right). The structure consists of chains which have a threefold screw symmetry.

3. Experimental

3.1 Basics of (ultrafast) DSC

In this section a brief explanation is given of regular Differential Scanning Calometry (DSC) and key differences between regular and ultrafast DSC (such as the Mettler-Toledo Flash DSC 1 that is used in the present research). A DSC is able to measure the heat flow of a sample when it is heated, cooled or kept at a constant temperature³². This is done by measuring the heat flow of two crucibles or pans (Figure 5) of which one contains the sample. Ideally, the difference of the two pans is measured so that only the processes that happen in the sample contribute to the end signal. In practise however, many other factors influence the environment such as the heat capacity of the sensors and the atmosphere around the sensors. This is why the Flash DSC uses a feedback system to regulate its temperature.

The sample mass will require a certain heat flow because of its heat capacity. This enables observation of transitions that change the heat capacity like glass transition as well as endothermic or exothermic processes like crystallization or melting. The crucibles are closed and therefore the temperature inside is relatively homogeneous. Furthermore, no material can evaporate from the crucible, and degradation due to air can only be due to the small amount of air in the pan when it was sealed.

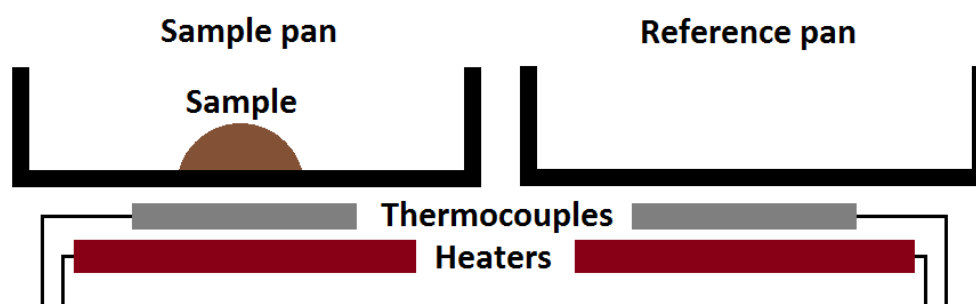


Figure 5: Schematic overview of a differential scanning calorimetry (DSC) setup. There are two pans, one which is used for to measure the heat flow of the sample and one that measures the heat flow without a sample and is used as reference.

For a normal DSC heating and cooling rates can go up to 1 K/s while for a Flash DSC the heating rate can reach 40.000 K/s and the cooling rate 4000 K/s¹⁴. This makes it possible to investigate phase change materials since a high cooling rate is required for them to become amorphous. Unlike normal DSCs which have two small pans, the Flash DSC has a sensor chip on which the samples are placed (Figure 6). While in normal DSC the sample masses can be in the order of mg, in a Flash DSC these masses are below a μg . The area around the sensor is flushed with a nitrogen flow of 20 ml/min which prevents oxidation of the sample during heating. In addition, the metal clamping the sensor can be cooled down to $-90\text{ }^{\circ}\text{C}$ allowing a fast removal of heat from the sample and thus a fast quenching down to room temperature. Note that the sensor cannot be treated as a closed system without thermal gradients. Because of the (limited) heat contact between the sensor and the sample and the thermal gradient in the sample as a function of distance to the sensor surface, the temperature in the sample can lag behind. It is shown however, that for heating rates lower than 1000 K/s the thermal lag will be below $5\text{ }^{\circ}\text{C}$ ³³.

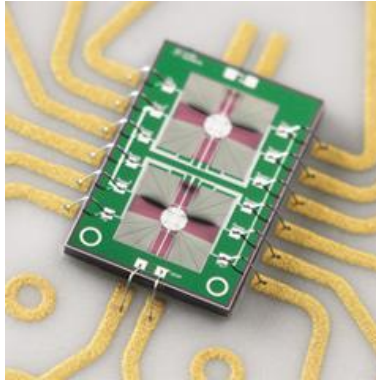


Figure 6: The underside of the chip that is used in the Flash DSC to measure samples. There are two areas in the centre, one where the sample can be placed and the other one that is used as reference.³⁴

3.2 Making samples and performing experiments with Flash DSC

The alloys that are measured in the Flash DSC have to be made first. This is done by vacuum sealing the individual components into a quartz tube. The quartz tube is then placed in an oven where the individual components melt. After that, the quartz tube cooled to room temperature such that a homogenous ingot remains. In this research one ingot of $\text{Se}_{45}\text{Te}_{45}\text{As}_{10}$ and one ingot of $\text{Se}_{45}\text{Te}_{45}\text{Sb}_{10}$ were made and used.

To obtain sample material for the Flash DSC, some material is scraped of the alloys by using a knife. The sample material is then selected under the microscope based on size and is placed on the sample side of the Flash DSC sensor by using a hair on a pencil. Before any experiments are done, the sample material is heated at 100 K/s to 450 °C and cooled at 4000 K/s back to room temperature several times until the heating curves deviate less than 5% from each other. This procedure melts the sample onto the sensor which improves the thermal contact between the sensor and the sample. It also avoids any irreversible processes like the change of shape that occur when the sample is molten at the first few Flash DSC experiments. To do experiments with the Flash DSC, heating schemes are made which describe how the temperature should change in time.

During the DSC experiments the sample alloy can evaporate partly. Since the melting temperature of selenium is much lower than of tellurium, arsenic and antimony it will evaporate in a larger extend. This makes it possible to do the measurements on a range of compositions as long as the evaporation during the measurements is not too large to influence the measurements itself. Figure 7 shows two heating schemes used in this research, one to measure at different heating rates and the other one to measure at different cooling rates. A control measurement is shown red, the measurement itself in blue.

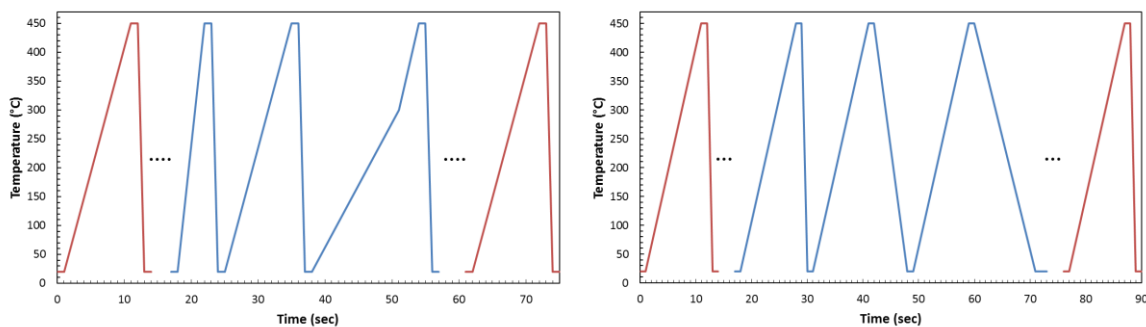


Figure 7: Heating scheme to measure at different heating rates (left) and different cooling rates (right). A control measurement is shown red, the measurement itself in blue.

Both heating schemes start and end with a control measurement, a ‘melt-quench’ where the sample is heated to 450 °C at a heating rate of 100 K/s to melt the sample and quenched with 4000 K/s to make the sample amorphous. These melt quenches can then be compared to determine if the sample changed during the measurement. For the experiment with different heating rates the sample is heated to 450 °C at different heating rates and then cooled at 4000 K/s to make the sample amorphous again. At heating rates below 100 K/s, the heating rate is changed to 100 K/s above 300 °C. This is done to prevent the sample from evaporating too much. For the experiment with different cooling rates the sample is heated at 100 K/s to 450 °C and cooled with different rates afterwards. Between the heating and cooling curves there is always an isothermal segment of 0.1 second to allow the temperature to stabilize. By doing the experiment with different cooling rates it is possible to determine the lowest cooling rate which does not show crystallization. This is called the critical quench rate and it is also dependant on the samples composition.

It is also possible to do isothermal measurements with the Flash DSC. However, since the sensitivity of the heat flow measurement is directly dependent on heating rates (and as such very insensitive on longer time scales) the information has to be obtained from heating curves that follow after the isothermal segment. There are two parameters that can be changed for the isothermal segments: the time and the temperature. Since at higher temperatures the evaporation rate of the samples becomes too high, the experiments done in this research are done at much lower temperatures than the melting temperature with varying isothermal times as shown in Figure 8.

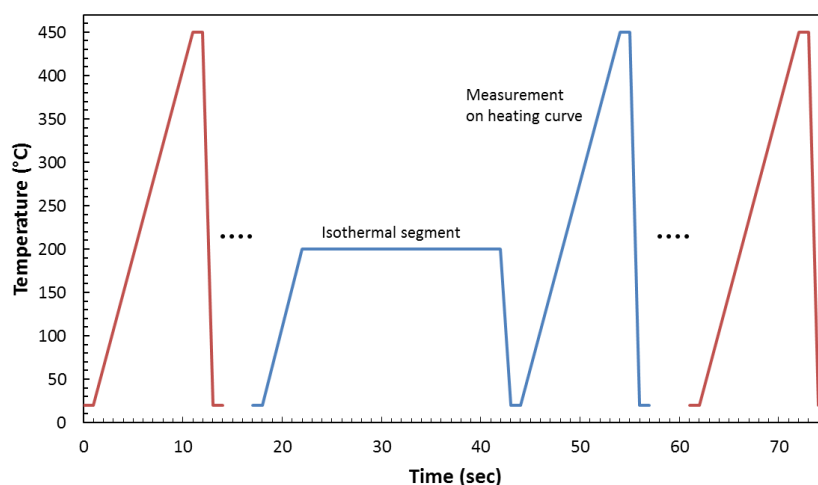


Figure 8: The heating scheme of isothermal measurements. Again, the measurement starts and ends with a melt quench. The isothermal segment can vary in temperature and time. The changes are measured on a melt quench after every isothermal segment.

Again, before and after the whole measurement a melt quench is done to compare the sample state. Then several measurements are done where the sample is heated at 100 K/s to the isothermal temperature where it remains constant for a set time. After that the sample is cooled at 4000 K/s to room temperature and reheated to at 100 K/s to 450 °C. On this heating run the state of the sample is measured and the sample is brought again in the melt to remove the thermal history. Last, the sample is cooled with 4000 K/s to make the sample amorphous for a new isothermal measurement.

Another experiment that is done, is heating the sample at a low cooling rate to a certain temperature, cooling it and finally reheating it back to 450 °C with 100 K/s (Figure 9). Later on, experiments show that at these low heating rates another transition is starts showing up. This experiment allows to measure how the heat capacity changes during this transition.

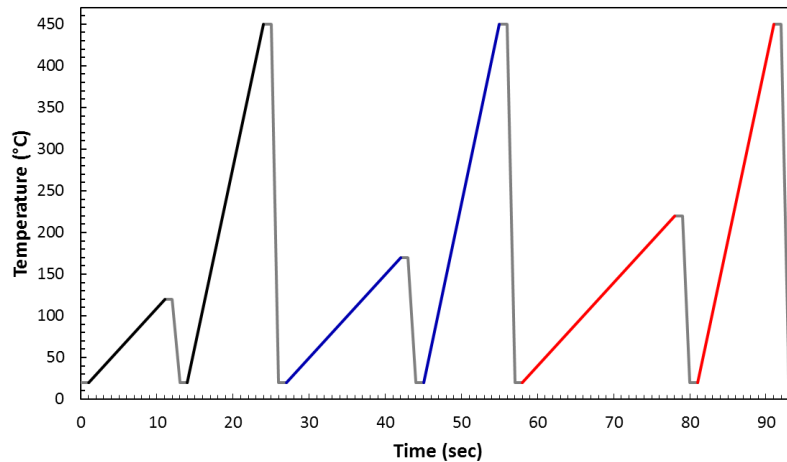


Figure 9: A heating scheme where the sample is first heated with a low heating rate to a certain temperature and then with a heating rate of 100 K/s to 450 °C . This is repeated for several temperatures to which the first heating runs are heated to see how the heat capacity changes during the transitions on the low heating rate curve. The cooling rates used are -4000 K/s.

On the heating and cooling segments there are several transitions that are expected to be measured using DSC. First of all, a crystallization peak is expected which is a first order transition. The crystallization temperature is determined by taking the maximum of this peak. Furthermore, a glass transition, which is a second order transition, can occur when the material is amorphous. The glass transition is determined by taking the middle point of the intersection of the steepest tangent on the onset/offset interval and the onset and offset tangents (Figure 10). Last, if the material is crystalline it will melt at a higher temperature which is also a first order transition. The melting temperature is determined by the intersection of the steepest tangent in the melting curve and the tangent at the onset which hits the offset at its highest point . Moreover, the crystallization or melting energy can be obtained by integration the peak. To do this the baseline is fit by using a spline. When the material fully crystallizes, the crystallinity can be determined by taking the fraction of the crystallization energy on a heating curve and the crystallization energy of a heating curve that went from amorphous to crystalline. This assumes that the material fully crystallizes which does not necessarily have to be the case. However, this method still provides a useful insight for the amount of crystallized material compared to the amount of crystallization that can be achieved.

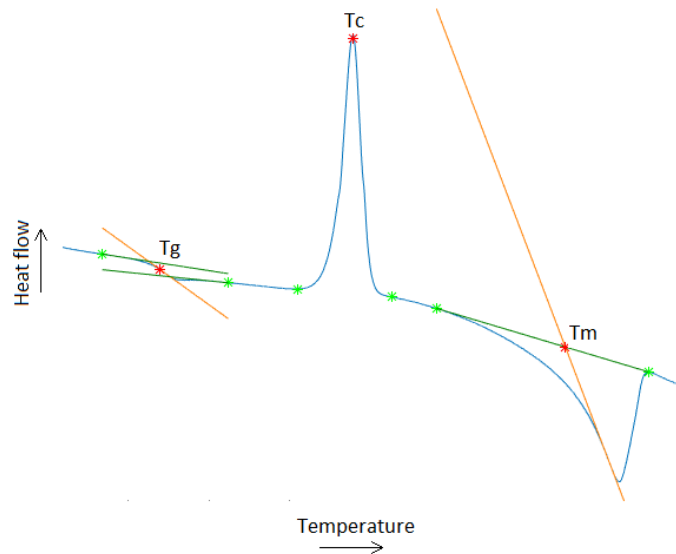


Figure 10: The glass transition temperature (T_g), crystallization temperature (T_c) and melting temperature (T_m) for the heat flow of a possible DSC curve. The light green stars indicate the onset and offset taken, the dark green lines are the slopes at these points and the orange lines are the steepest tangents on the onset/offset interval.

To crystallize a sample for microscopy a relatively simple heat scheme is used which consists of one melt quench to reset any thermal history followed by a heating run where the crystallization occurs (Figure 11). The melt quench is always done up to a temperature of 450 °C. Crystallization from the amorphous phase is done by heating the sample to above crystallization peak. In the Flash DSC this is done by using a heating rate of 5 or 100 K/s and a cooling rate of 4000 K/s while in the DSC a heating rate of 0.5 K/s and a cooling rate of 1.7 K/s is used. Also, crystallization from the melting phase is done in the Flash DSC where the sample is heated with 100 K/s to 450 °C and then cooled with 100 K/s to room temperature.

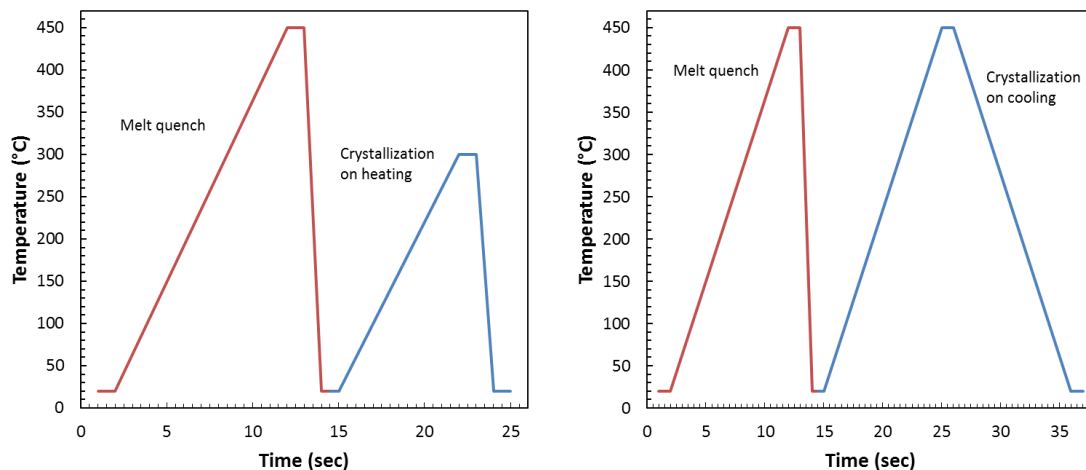


Figure 11: Heating schemes to crystallize the sample from the amorphous phase (left) or from the melt (right). The melt quench in red is done to reset the thermal history of the sample.

Samples that are made by the normal DSC are large enough to be polished to be measured optically or by SEM. This is done by first placing the samples in epoxy and then grinding and polishing them until the surface is smooth enough to be measured in SEM. The steps to create TEM samples from Flash DSC treated samples are more extensive and therefore explained in section 3.4.

3.3 Microscopy

For this research several types of microscopes are used (Figure 12). To obtain optical overviews of the samples, an optical microscope was used to obtain images with a magnification of 50 to 1000. To obtain images at higher magnification Scanning Electron Microscopy (SEM) is used. This is a microscope where electrons are shot at a sample to produce a signal caused by the electron-sample interactions. The image can then be produced by detecting either secondary electrons (SE) or backscattered electrons (BSE). Furthermore, the electrons can induce X-ray radiation in the sample which can be used to measure for elemental analysis of the sample, this method is called Energy-Dispersive X-ray Spectroscopy (EDS). The spectra that are measured are fit by using the NSS software of Thermo Scientific to obtain the atomic weight percentages of the elements in the sample. Since backscattered electrons and X-ray imaging are influenced by the samples surface characteristics it is required to grind and polish the samples. The SEM samples are made by embedding the sample in epoxy. To prevent charge build-up in the sample, a conductive layer is added to the SEM samples which is in this case a sheet of copper that has contact with the sample itself. To measure the TEM samples that are discussed in section 3.4 in the SEM, a thin gold layer is sputtered onto the sample to act as conductive layer.

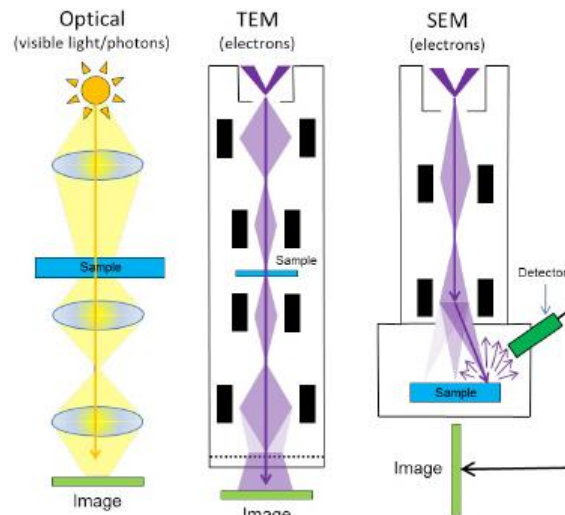


Figure 12: A schematic overview of an optical microscope (left), Transmission Electron Microscope (middle) and Scanning Electron Microscope (right).³⁵

For even higher resolution and information about the atomic structure Transmission Electron Microscopy (TEM) is used. For this type of microscopy the electrons are directed by a lens system through the sample. The image is then caused by the interaction of electrons with the sample and can be observed on a phosphor screen below the sample or be recorded by a CCD camera. Since the electrons have to penetrate through the sample it is required that the sample is very thin (below ~ 100 nm). Similar to SEM it is also possible to do EDS since the electrons will also induce X-ray radiation in the TEM sample. Additionally, it is possible to focus the electron beam into a probe that scans over the sample to obtain an image; this is called Scanning Transmission Electron Microscopy (STEM). Combined with EDS it is then possible to create an elemental map of the sample. The TEM images were obtained by a JEOL 2010. This electron microscope contains a LaB_6 crystal that acts as the electron source. The images were recorded using 200 keV electrons and a beam current about $5 \mu\text{A}$ in a vacuum of about 10^{-7} mbar.

3.4 Sample preparation: from Flash DSC to electron microscope

One of the main goals of the present research has been to transfer a sample that has been thermally treated and investigated in the Flash DSC to an SEM or TEM to measure the structure. This is not trivial since the sample has a thickness of approximately 50 μm and moreover, it is molten onto the sensor after treating it in the Flash DSC. To measure the sample in the TEM it has to be put in a support of 3 mm diameter and thinned to below 100 nm to make the sample electron transparent. There are basically three steps in this process: removing the sample from the Flash DSC, placing the sample in a support and ion milling the sample until it is thin enough using a Precision Ion Polishing System (PIPS). During this process, when the sample is polished in the ion mill, it is possible to investigate the sample in the SEM. A step by step recipe is listed below.

Required materials

- Thin and thick hair on a pencil
- Tungsten needle
- Tweezer, thin tips, reverse action
- A very small piece of tissue that is twisted to create a tissue tip
- TEM copper grid to store samples on
- Small material flakes (SeTe/SeTeAs)
- Silicon oil
- Two round 3 mm copper TEM rings with a hole diameter of 1 mm
- Two-component glue (Power Epoxy)
- Wooden tooth picks
- Two small glass plates with a similar size as the TEM ring

Moving the sample from the Flash DSC sensor

1. Before doing thermal treatments with the Flash DSC, use a thick hair to put silicon oil on the sample sensor.
2. Place the sample onto the sensor.
3. Perform the required Flash DSC measurements.
4. If necessary, use the thick hair to pull the sample loose from the sensor keeping it on the sensor.
5. Use the small piece of rolled up tissue to pick up the sample.
6. Scrape the sample onto a TEM grid.

The silicon oil will prevent the sample from sticking to the Flash DSC sensor. However, the oil will evaporate during measurements thus if too many measurements are done the sample can still stick to the sensor surface. In this case it is usually possible to peel the sample loose using a thick hair, if not more oil has to be added during the measurements. The easiest way to pick the sample up with the tissue is to push it into the sample such that a larger area of the tissue surrounds the sample. After this, the TEM grid should be carefully handled to prevent the sample from falling off (Figure 13).

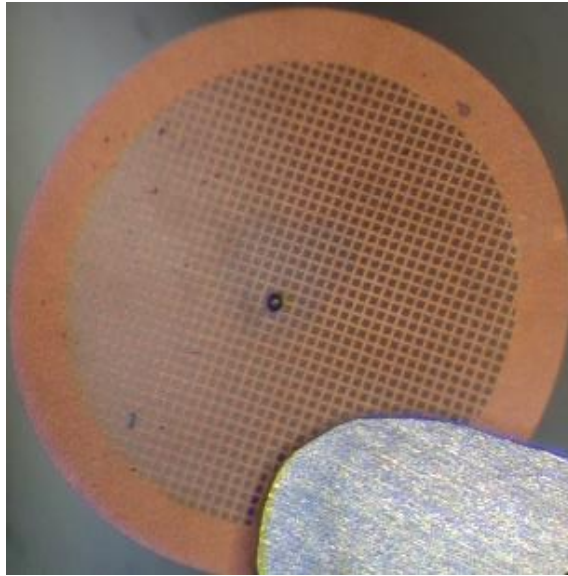


Figure 13: TEM grid which contains a sample that is taken from the Flash DSC in the centre. The grid has a 3mm diameter, the sample is estimated to have a lateral size of about 50 μm .

Creating a sample support

1. Pick up a sample using a hair and place it carefully aside.
2. Pick up a TEM ring with a tweezer and put it under the microscope.
3. Mix the Power Epoxy glue using a tooth pick until it becomes transparent.
4. Use another tooth pick to pick up a very small drop of glue by gently touching the glue.
5. Move the tooth pick through the hole of the TEM ring so it will leave a layer of glue.
6. Check the thickness of the glue layer by holding it sideways under the microscope. If there is too much glue, repeat step 2 – 4 for a new ring.
7. Rotate the copper ring by 180 degrees.
8. Place the sample into the glue using a hair.
9. Move the sample to near the centre using a thin hair until the glue is hardened enough to prevent the sample from moving.
10. Wait until the glue is fully hardened.

Since the glue will harden when it's placed in the ring, it is necessary to put the sample on a hair before applying glue. It is advised to work above a sheet of aluminium foil so that when the sample falls off it is possible to retrieve it. The amount of glue that is applied in the ring has to be as little as possible since it has to be ion milled later on. Also moving the tooth pick through the ring instead of touching the ring will prevent the glue from spreading to the sides of the ring instead of creating a small layer. To estimate the thickness, the side of the copper ring can be taken as indication which is 50 μm thick. Since the glue will be slightly thicker at the side that it was applied, the ring is rotated so that the sample lies better centred in the perpendicular direction. It will generally take at least one hour for the glue to harden. An example of two samples inside a copper-glue support is shown in Figure 14.

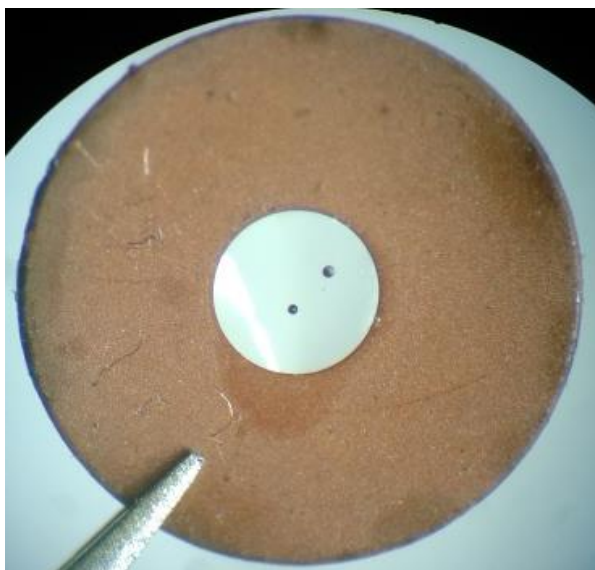


Figure 14: TEM ring containing a thin layer of glue in which two samples of the Flash DSC are placed.

Ion milling the sample

1. Align the PIPS if necessary such that the ion guns focus properly on the center of the ring/hole.
2. Place a glass plate in the PIPS holder, put the sample on top of the glass plate and place a copper ring on top of that.
3. Ion mill the sample in the PIPS using 4 keV, dual modulation, top-top gun configuration at 5 - 7° until the sample becomes shiny.
4. Remove the glass plate and copper ring from the stack.
5. Rotate the sample 180° and repeat step 2 – 4 for the other side.
6. After step 5 it is possible to measure the sample in the SEM.
7. Ion mill the sample in the PIPS using 2 - 4 keV, dual modulation, top-bottom gun configuration at 5 - 7° until a hole appears. Generally, the hole starts somewhere in the glue.
8. Ion mill the sample in the PIPS using 2 - 4 keV, dual modulation, top-bottom gun configuration at 5 - 7° until the hole edge reaches the sample. This should be done more carefully than step 7.
9. Polish the sample in the PIPS using 0.5 – 2 keV, dual modulation, top-bottom gun configuration at 5 - 7°.
10. The DSC sample now has a thin electron-transparent wedge next to the hole and can be investigated using TEM.

For the ion milling the PIPS 2 of Gatan is used. This system sputters argon ions from two guns to polish a sample. Since it is unknown how much glue there is on each side of the sample it has to be shot from one side to mill away the glue until the sample becomes shining as shown in Figure 15. To prevent redeposition, a glass plate is placed on the other end of the sample. Since the copper ring can be damaged during the process a spare copper ring is added on top of the sample. The glass plate and copper ring can be removed by using tweezers and/or a tungsten needle. Since the glue is not perfectly flat but thicker in the center, the hole will not form at the center but slightly to the side. Especially when the hole almost reached the sample it is possible that the glue near the sample is thin enough to form a smaller hole before the large hole reaches the sample. This is why the last steps should be done more carefully by ion milling at lower energies and smaller time intervals.

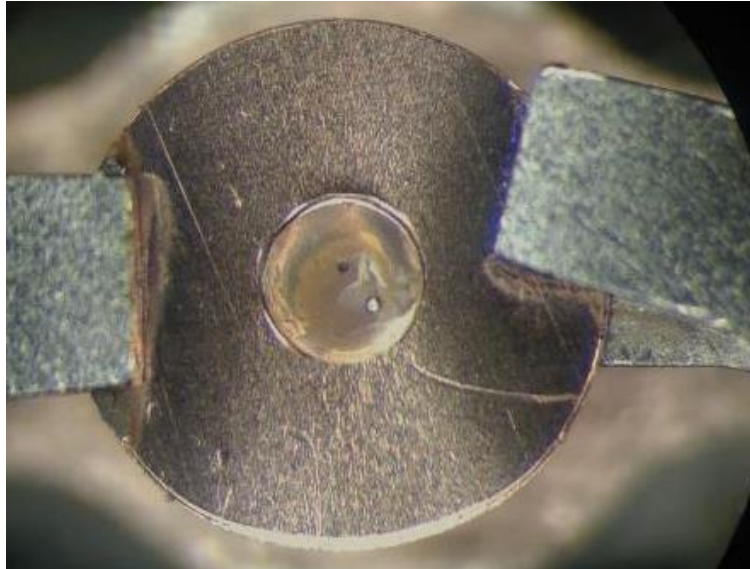


Figure 15: The same samples as Figure 14, now clamped on both sides by the PIPS holder. The top has been ion milled such that the glue is sputtered away from the bottom right sample (which is shiny). The sample in the centre is still covered by glue.

4. Results and discussion

4.1 Structure of (heat treated) SeTe

To investigate the structure of SeTe, an ingot has been made with a composition of 25 at.% selenium and 75 at.% tellurium. The ingot has been made as described in the method section thus the structure of the ingot is formed on slow cooling from the melt. Optical and SEM images of this ingot are shown in Figure 16.

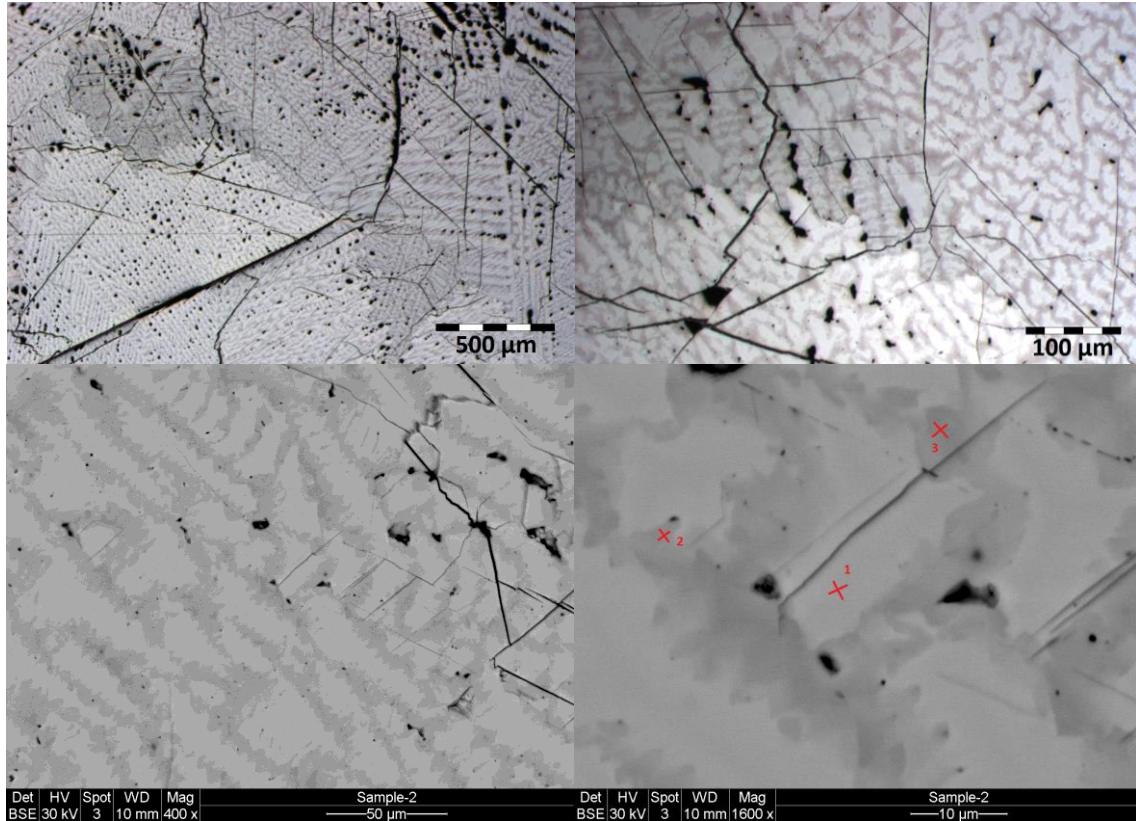


Figure 16: Optical (top) and SEM (bottom) images of the SeTe ingot sample at different scales. All images show bright lamella. On the bottom right SEM images several spots are shown on which SEM EDS has been performed.

The images shows bright lamella that have sizes in the order of 10 μm and seem to be grouped in grains that are in the size order of millimeters. The boundaries of these lamella are not straight, there is a gradual color decay. SEM EDS has been performed on several spots as shown in the right bottom image of Figure 16 from which the results are shown in Table 2.

Spot	Se (at.%)	Te (at.%)
1	71.0	29.0
2	80.6	19.4
3	86.6	13.4

Table 2: The results of the SEM EDS measurements that are done on the spots shown in Figure 16. The contrast in the image seems to be due to a difference in composition.

The SEM EDS measurements show that the contrast in Figure 16 is due to a difference in composition. The ingot sample was formed under uncontrolled condition. A piece of the ingot was crystallized in the Flash DSC by the method described in the method section with a heating rate of 100 K/s up to a temperature of 255 $^{\circ}\text{C}$ (Figure 17).

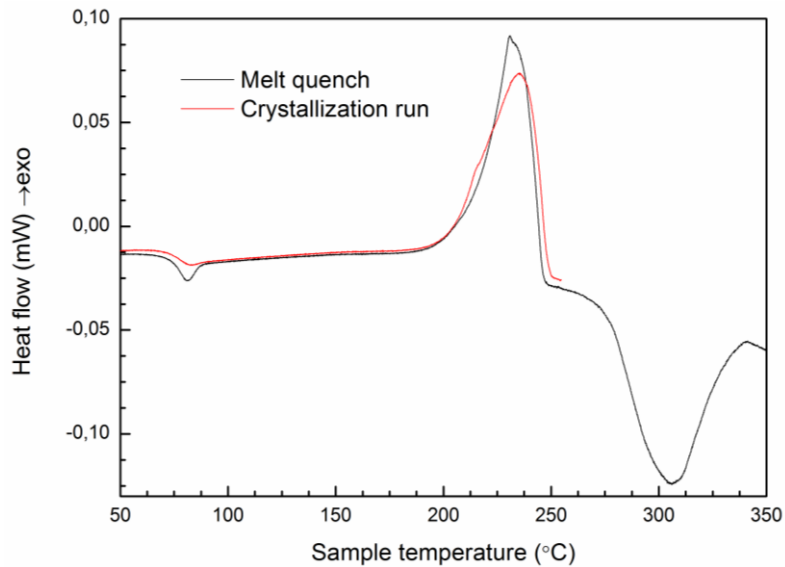


Figure 17: The heating curves of the SeTe sample that was prepared for the TEM. The melt quench is done to a temperature of 350 °C to reset the thermal history. The second curve (crystallization run) is done to crystallize the sample up to a temperature of 255 °C. The melting and crystallization energy is 55 μ J, the crystallization temperature is 231 °C and the melting temperature is 276 °C.

On the first melt quench run, which is meant to reset the thermal history, there is a dip in the glass transition visible which is due to enthalpy relaxation. The crystallization energy measured on the crystallization run is 55 μ J which is equal to the melting energy that is measured on the melt quench. Furthermore, the crystallization temperature is 231 °C and the melting temperature is 276 °C. The composition that is inferred from the melting temperature is 30.3%. This means that about 5 at.% selenium has been evaporated during the Flash DSC measurements. Next, the sample is turned into a TEM sample as described in the method section. The overview images are shown in Figure 18.

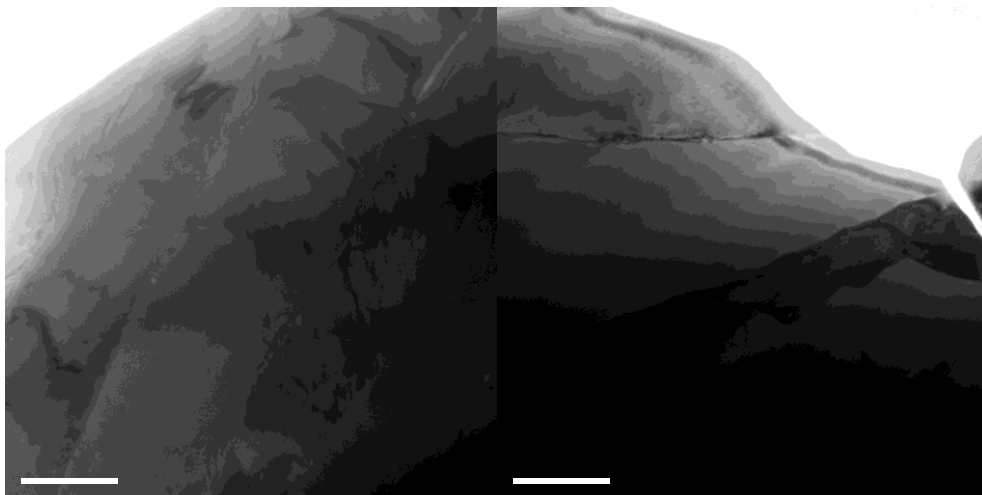


Figure 18: Overview images of a SeTe sample that was crystallized in the Flash DSC at 100 K/s. The images show lamellae that are in the size order of 0.1 – 1 μ m.

The overview images show areas where there are long crystal domains (lamella) visible in the size order of 0.1 – 1 μ m. When the images are rotated, the domains shift in color which indicates that there is no amorphous material present. This is supported by the diffraction patterns that are taken, there are no amorphous rings found (Figure 19).

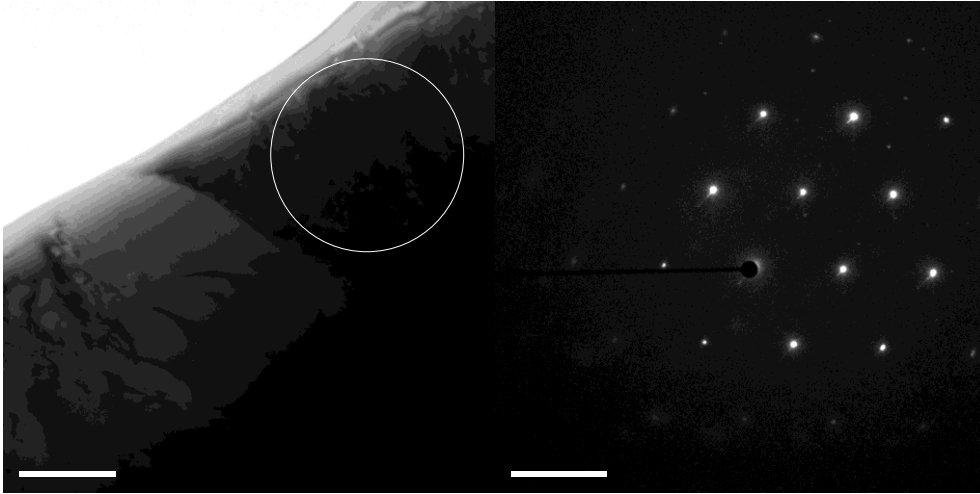


Figure 19: The diffraction pattern of a crystal area in the heat treated SeTe sample. The diffraction patterns taken are consistent with the trigonal crystal system and $P\bar{3}_121$ space group described in the theory.

From the diffraction patterns the lattice parameters a and c can be inferred which are 4.411 ± 0.031 and 5.270 ± 0.038 , respectively. This is consistent with Vegard's law for $\text{Se}_{70}\text{Te}_{30}$, assuming the composition obtained from the Flash DSC results, by which the lattice parameters are calculated to be 4.394 and 5.250 for a and c , respectively. This composition has also been measured by TEM EDS for the same areas as the diffraction patterns were taken and are shown in Table 3. The values measured by TEM EDS are within the 3 at.% error compared to the values inferred by ultrafast DSC.

Method	Se (at.%)	Te (at.%)
Ultrafast DSC	69.7	30.3
TEM EDS	72.0 ± 3	28.0 ± 3

Table 3: The composition which has been inferred from Flash DSC as well as measured by TEM EDS.

4.2 Thermal properties measured by DSC of SeTeAs

In this section, the thermal properties of SeTeAs, as measured by Flash DSC, are analysed and discussed.

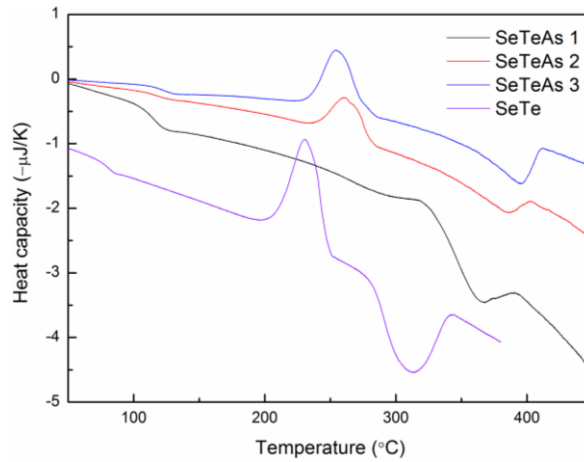


Figure 20: The heating curves at 100 K/s for three SeTeAs samples and a SeTe sample normalized to the heating rate and including an offset for clarity. SeTeAs sample 1 is measured just after it was molten on the sensor while SeTeAs sample 1, 2 and the SeTe sample are measured after some composition degradation. The main difference is in the melting onset which is longer and less sharp for SeTeAs than SeTe.

As can be seen in Figure 20, a pristine sample (SeTeAs 1) will start crystallizing at a relatively high temperature and at 100 K/s the melting starts before crystallization completes. While doing measurements, the composition shifts which decreases the crystallization temperature. This separates the crystallization peak from the melting peak and therefore makes it possible to perform more accurate measurements at higher heating rates. There is a difference in peak height and slope for the different samples because the samples have a different (and unknown) mass. All SeTeAs samples show a similar melting behaviour though, one with a long onset and a sharper offset than SeTe. This long onset and also the initial overlap in crystallization and melting peaks make it more difficult to determine the onset of the melting peak for SeTeAs.

As mentioned shortly in the method section, mainly selenium evaporates from the specimen during the Flash DSC experiments which means that the sample can be measured over a range of compositions.. Since the relation between the melting temperature and composition of $\text{Se}_x\text{Te}_{1-x}$ is well known (Appendix A, phase diagram SeTe), it is also used to calculate the ratio of SeTe in the SeTeAs. This gives the following relation for the composition ratio $C = \text{Te}/(\text{Se} + \text{Te}) \cdot 100\%$ which will be denoted as percentages unless told otherwise:

$$C = -0.00047 * T_m^2 + 0.7459 * T_m - 139.8104 \quad (5)$$

It is assumed that the As does not influence the melting point significantly. To verify this, the composition of the samples was inferred by Formula 5 and measured by SEM-EDS or TEM-EDS afterwards (Figure 21). For SEM-EDS, the Flash DSC sensor including sample was placed directly in the SEM while for TEM-EDS the samples were removed from the sensor and then placed in the TEM.

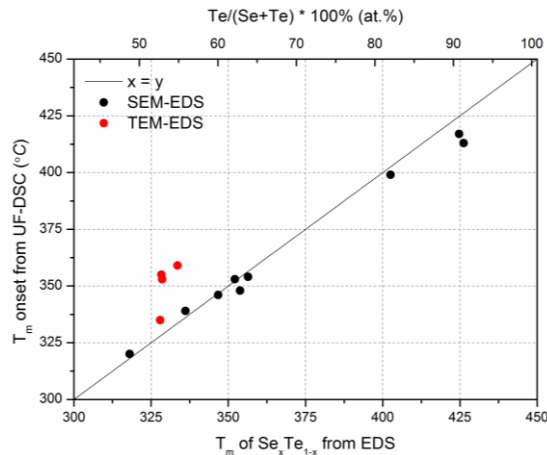


Figure 21: The correlation between the melting temperature of SeTeAs measured in the Flash DSC and the melting temperature calculated from the composition which is measured in the EDS for the same Flash DSC samples. For the calculation of the melting temperature the binary phase diagram is used for SeTe. The measured points deviate less than 10 °C or 2.5 % from the line thus the influence of arsenic is not largely significant on the melting peak temperature.

If the As does not have any influence, the data points should lie on a straight line for which the melting temperature measured by the Flash DSC and melting temperature inferred from the EDS composition is the same. For the samples measured by SEM-EDS, the deviation of the data points from this line is maximally 10 °C or 2.5 %. This shows that the influence of As is indeed not large. However, the samples measured by TEM-EDS show a larger deviation which is maximally 30 °C or 10 %. A reason for this could be that the samples measured by TEM-EDS were smaller than the samples measured by SEM-EDS which could make the determination of the melting peak more difficult. Another difference is that the samples measured with TEM-EDS were ion milled in the PIPS. This could heat the sample by which selenium was evaporated or there could be preferential sputtering which causes a reduced selenium ratio.

4.2.1 Heating rates and composition

The SeTeAs sample has been investigated using different heating rates as described in the experimental section 3.2 Figure 7, a representative set of resulting DSC curves is shown in Figure 22. All curves are normalized to the heating rate.

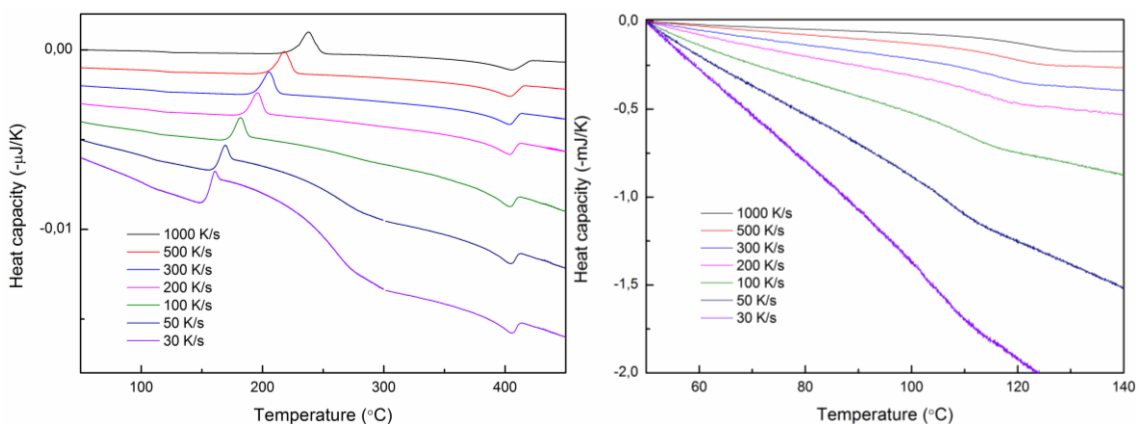


Figure 22: Several heating runs on SeTeAs for different heating rates (left) and a zoom in on the glass transitions (right). All data is normalized to the heating rate and have an offset to prevent the curves from overlapping. Above all heating rates above 300 °C are changed to 100 K/s if they are lower than 100 K/s. This causes a large onset peak which is removed from the graph (a white linebreak is displayed). The curves show that at lower heating rates a new transition starts showing up.

Because the curves are normalized to the heating rate, not all glass transitions are visible in the graph, but the transition is present at all heating rates. For lower heating rates a second transition becomes visible which comes after the crystallization peak. At some point the crystallization peak and this transition overlap each other so much that they are both indistinguishable, which is in this case below 30 K/s. The heating rate at which this second transition starts showing up differs from sample to sample. When the composition shifts to higher Te% due to evaporation, the second transition can be observed for increasingly higher heating rates. To see how the heat capacity changes the heating scheme shown in Figure 9 is used where the sample is heated with a heating rate of 3 K/s to a certain temperature and then reheated with 100 K/s to 450 °C, the results are shown in Figure 23.

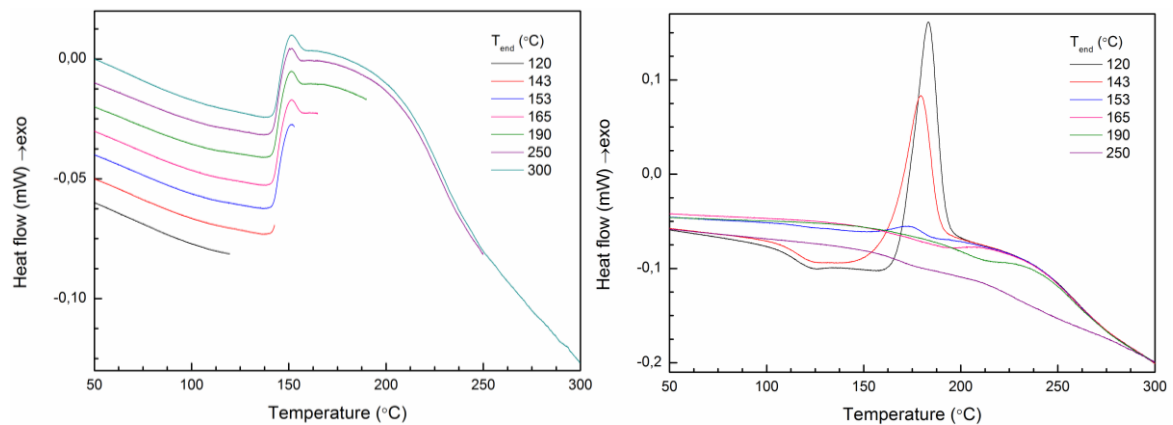


Figure 23: Each time the sample is heated at 3 K/s to a certain temperature, which gives the heat flow as shown in the left graph. After each heating run it is then reheated at 100 K/s to 450 °C which is shown in the right graph. The results show that the heat capacity decreases during crystallization at 3 K/s and increases back to its original value afterwards in a transition that occurs after crystallization.

Heating to before the crystallization peak (the black line in Figure 23 left) shows a crystallization peak as expected in the heating run after (the black line in Figure 23 right) as expected. When the sample is heated to above the crystallization temperature (143 °C in this case), the heat capacity is decreased afterwards as shown in the 100 K/s heated run after. Next, when the sample is heated to a higher temperature (250 °C in this case) another transition occurs that increases the heat capacity in the 100 K/s heating run afterwards back to its original value (when the material was amorphous). Since most heating runs that are done at 3 K/s don't go through this transition that increases the heat capacity, the transition is also visible for most of the 100 K/s heating runs. To summarize the above, during the crystallization at low heating rates and/or low crystallization temperatures, a process occurs which decreases the heat capacity. Another transition then occurs at higher temperatures where this heat capacity is increased back to its original value.

To construct an extended phase diagram, the melting temperature is used to calculate the composition. However, in some cases the melting temperature overlaps with the crystallization temperature by which the melting temperature cannot be determined properly and therefore deviates much as shown for a SeTeAs sample in in Figure 24 (in this case the 500 K/s and 200 K/s had this problem).

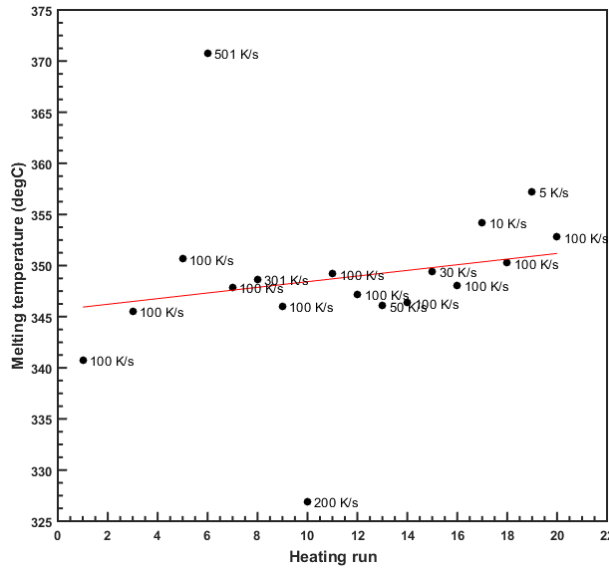


Figure 24: The melting temperatures for a set of heating experiments including their heating rate. The experiments were done with a heating rate that is shown up to 300 °C, after that the sample was heated with 100 K/s or higher to 450 °C and quenched with 4000 K/s. The melting temperatures at 200 and 500 K/s could not be determined properly due to an overlap in crystallization and melting peak. Therefore, the melting temperature is interpolated using a linear regression function as shown by the red line.

Since during the melting trajectory the heating rates are all 100 K/s or higher, the compositional shift for each heating run is estimated to be roughly the same for each heating run. Therefore the melting temperature is interpolated using a linear regression as a function of the amount of heating runs which is shown by the red line.

In Figure 25, the extended phase diagrams of SeTe and SeTeAs are shown in which the glass transition, crystallization temperature and the melting temperature are plotted for different heating rates and compositions. The SeTeAs samples were smaller than the SeTe samples which increased the amount of compositional shift during the measurements. The plot is shown for two different samples which have similar masses.

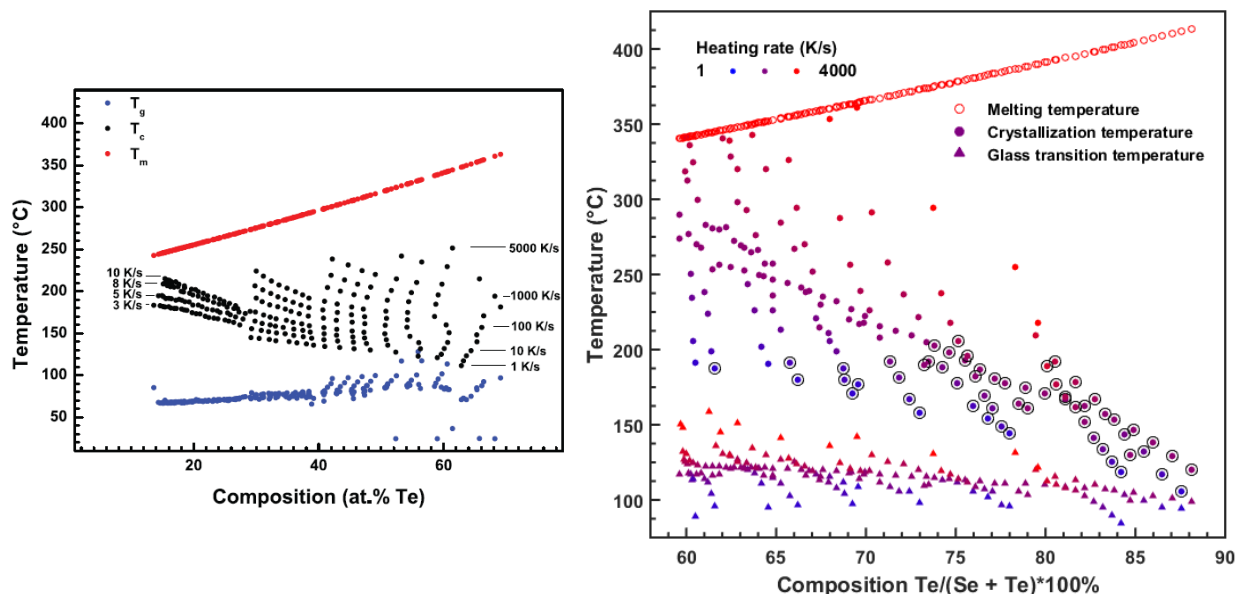


Figure 25: The extended phase diagram for SeTe (left) and SeTeAs (right) which shows the melting temperature, crystallization temperature and glass transition temperature for different heating rates and compositions. The crystallization peaks where the second transition was visible are marked with black rings. The colour indicates the heating rate which scales logarithmically from 1 K/s (blue/green) to 4000 K/s (red). For SeTe and SeTeAs, the measurements lie within the same

temperature range for similar heating ranges but in a different composition range. At 60% the crystallization temperature is about 100 °C higher for SeTeAs.²⁰

The main difference for SeTeAs when compared to SeTe is that the glass transition and crystallization temperatures are higher for the same heating rates. Thus by adding arsenic, the material becomes a better glass former. From 60% to 85%, the glass transition at 100 K/s decreases by 15 °C while the crystallization temperature at 100 K/s decreases by 110 °C. For higher Te concentrations above 87% the critical quench rate becomes too large. It would still be possible though to measure samples with a lower Se percentage by making ingots that contain less Se. The reduced glass-transition temperature, defined as $T_r = T_g/T_m$, gives an indication of how much undercooling is required for the material to become a glass and it is inversely proportional to the nucleation rate in a material³⁶. For SeTeAs this varies between 0.66 at 60% to 0.55 at 85% indicating that the nucleation rate increases for an increased amount of Te. The reduced glass-transition temperature of SeTe is 0.66 at 15% and 0.59 at 60% (Ref 6). Assuming that this ratio keeps decreasing with the composition, adding arsenic to SeTe increases the reduced glass-transition temperature.

Also shown in Figure 25 (right) are the crystallization peaks where the second transition (Figure 25 lower heating rate) becomes visible. This transition shows up at low heating rates below 220 °C. When the Te/(Se + Te) ratio increases the crystallization peaks occur at lower temperatures and the second transition also becomes visible at larger heating rates. This indicates that the second transition is not an artifact of the Flash DSC instrument, which is most sensitive at high heating rates.

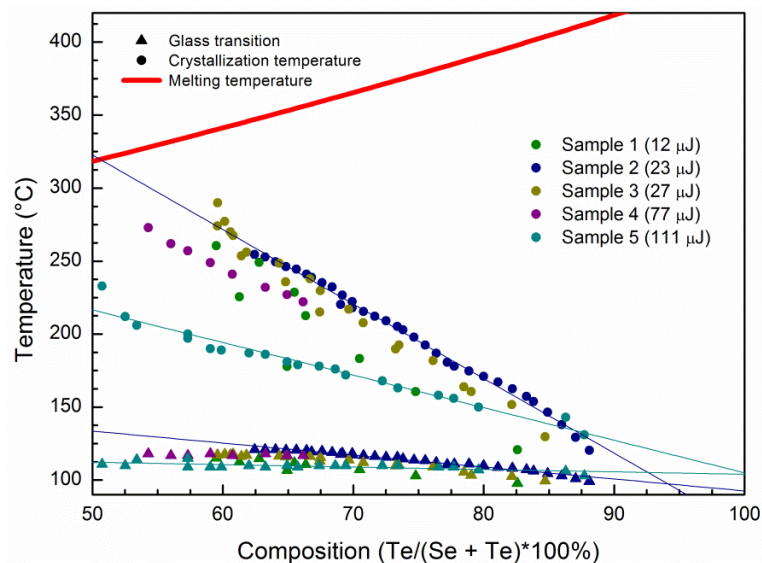


Figure 26: The glass transition, crystallization temperature and theoretical melting temperature at heating rates of 100 K/s shown for samples with different sizes. The energy of the crystallization peak at a composition of 65 % is given in the legend to give an indication of the size of the samples. A straight line is fit through the glass transition and crystallization temperatures. The intersection of these lines is at 94 and 100%.

In Figure 26, the glass transition temperatures and crystallization temperatures at 100 K/s are shown for five different samples with different sizes. Since the sample size could not be measured readily, the energy of the crystallization peaks (measured by taking an integral under the peak with a flat baseline) is given which is proportional to the crystallized sample mass. The sample with the lowest mass (sample 1) shows the largest spread, since the noise in the measurements is not larger than the other samples one possible explanation could be that this sample evaporates quicker which influences the measurement error. The other samples indicate that for a larger mass, the glass and crystallization temperatures become lower. Previous research on samples that were melt quenched

on the Flash DSC have shown the formation of crystals at the top of the sample due to thermal gradients in the sample³³. When this sample is reheated, the crystalline phase can grow from these crystals, which occurs much faster than when nuclei have to form in a fully amorphous material.

For sample 2 and sample 5 the glass transition and crystallization temperature are fitted using a linear regression which is extrapolated to higher ratios. The fit of sample 2 crosses at ratio of 95% and a temperature of ~ 100 °C while the fit of sample 5 crosses at a ratio of 100% and a temperature of ~ 105 °C. Since these intersects are not observed, the extrapolation could be invalid, but nevertheless it is expected that the crystallization temperature will stay above the glass transition temperature. The critical quench rate, which is the lowest cooling rate at which the sample did not show crystallization upon cooling from the melt, is shown in Figure 27 for both SeTe and SeTeAs.

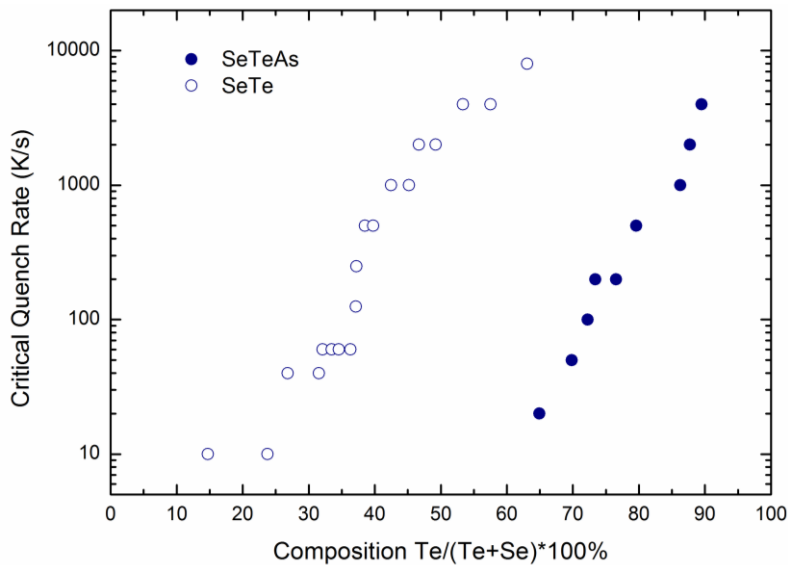


Figure 27: The critical quench rate for SeTe and SeTeAs for a range of $Te/(Te + Se)*100\%$ ratios. Both seem to be rising exponentially with the ratio $Te/(Se + Te)$. However the SeTeAs has a much lower critical quench rate thus it is a better glass former than SeTe.

As can be seen in the figure, for both SeTe and SeTeAs the critical quench rate is increasing as the amount of tellurium is increasing. This is as expected from the theory since tellurium is a better glass former than selenium. The critical quench rate for SeTe in the order of 10 K/s for 20 at.% Te to 10^4 K/s at 60 at.% Te. As for SeTeAs, the critical quench rate lies in the order of 20 K/s at 65 at.% Te to $6 \cdot 10^3$ K/s at 90 at.% Te. Thus by adding arsenic to SeTe, the material becomes a better glass former as was also indicated by the reduced glass-transition temperature.

4.2.2 Kissinger analysis

As described in the theory (section 2, Formula 3), Kissinger analysis allows determination of the activation energy of the crystallization process. Kissinger analysis is performed for the samples 2, 3 and 4 as shown in Figure 28. These samples are chosen because they all have data points in the range of 60 to 90 at.% Te.

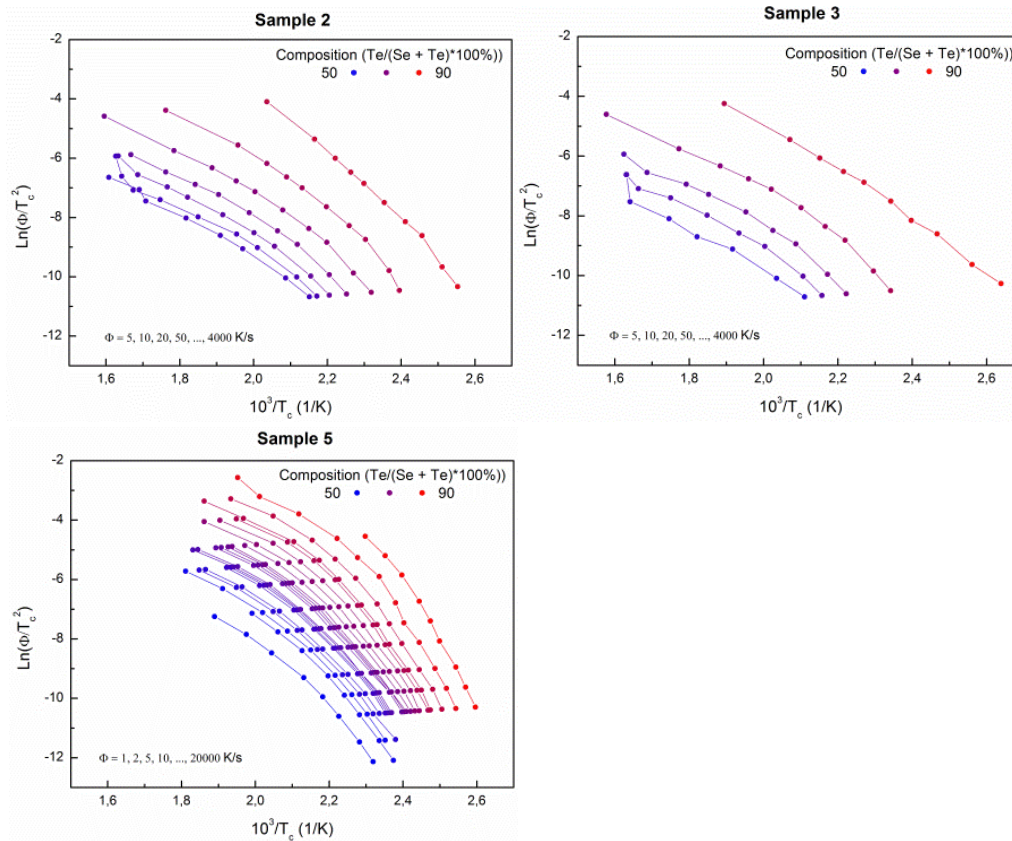


Figure 28: Kissinger plots for samples 2, 3 and 5 at different heating rates. The composition is indicated with a color that goes from blue to red for compositions from 50 to 90 Te/(Se + Te)*100%. The energies of the crystallization peak at a composition of 65 % are 23, 27 and 111 μ J for sample 2, 3 and 5 respectively. All samples show a curvature which indicates they do not follow the Arrhenius equation which is consistent with a fragile liquid.

The Kissinger plots are made for a range of compositions from 50 to 90 %. Each set of measurements that represent a line in the Kissinger plot had a compositional shift of 2 – 5 % for sample 2, 2 – 9 % for sample 3 and 2 – 7 % for sample 5. The degradation got larger after each run and was generally much smaller for the larger sample. For all samples there is a curvature present throughout all heating rates, thus in this case the Arrhenius equation does not hold, which is consistent with a fragile liquid. However, for the lower heating rates the curvature can still be approximated reasonably well with a linear (Arrhenius) fit, and the activation energy can be determined. The result is shown in Figure 29.

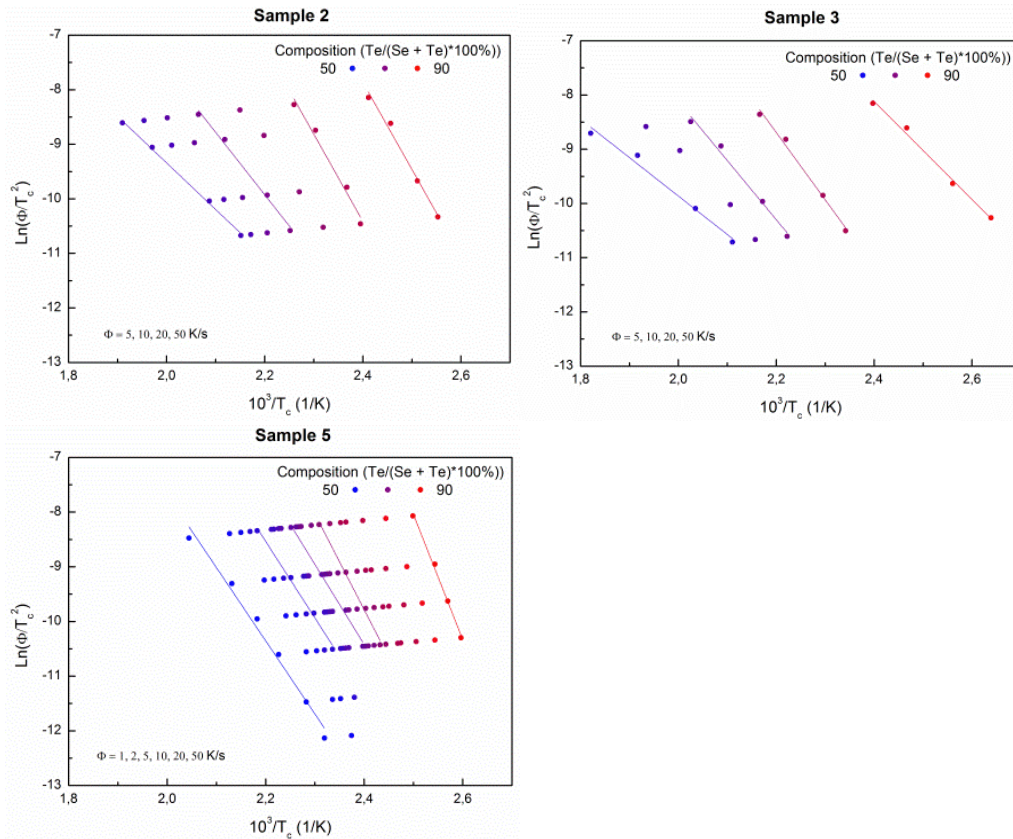


Figure 29: Linear fits for the Kissinger plots done at lower heating rates where the slope is approximately linear. For all samples there is an increase in slope for higher tellurium percentage. Only at the highest tellurium percentage in sample 2 and 3 this does not hold, which is because of the large shift in composition due to evaporation.

For these low heating rates the shift in composition was less than 2 %, this shift is considered small enough to be neglected. When there is a significant amount of composition shift during the measurement, the slope will be less steep and thus the activation energy that is fitted will be lower than the real activation energy. At higher concentrations of Te, this effect becomes more pronounced, since the sample has evaporated more material, and became smaller. Both effects decrease the signal to noise ratio and increase the amount of degradation per run. Thus, the fitted activation energy provides an underestimation of the actual value. The activation energy is plotted in Figure 30.

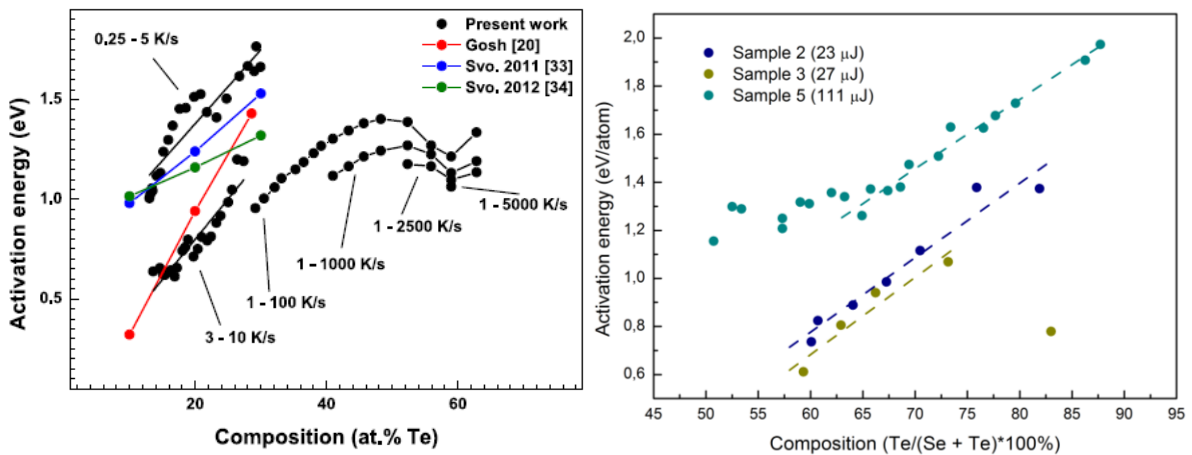


Figure 30: The activation energy shown for three samples with different masses as indicated by the crystallization energy. A linear fit is shown for data points above 60 %. The activation energy of SeTe lies between 0.5 and 2 eV in the composition range of 10 to 60% while the activation energy of SeTeAs lies within 0.5 to 2 eV in the range of 50 to 90%.²⁰

The activation energy of SeTe lies between 0.5 and 2 eV in the composition range of 10 to 60% while the activation energy of SeTeAs lies within 0.5 to 2 eV in the range of 50 to 90%. For SeTeAs, above 60 at.% Te the activation energy rises linearly for all samples with slopes of 0.031, 0.032 and 0.029 eV/at.%. The difference in absolute value can be contributed partly to that the composition shift in the large sample was lower. For a larger compositional shift, the slope becomes lower than the real slope and thus the activation energy becomes underestimated. This is also the explanation why the measurement at 82.5 % for sample 3 is much lower than the line on which the other data points lie. For higher Te concentrations the activation energy for crystallization increases. This seems counterintuitive since the extended phase diagram shows that crystallization occurs at lower temperatures for higher Te concentrations. However, crystallization is an exothermic process (Figure 31), therefore this shows that the Gibbs energy which is released during this crystallization is increasing faster than the activation energy.³⁷

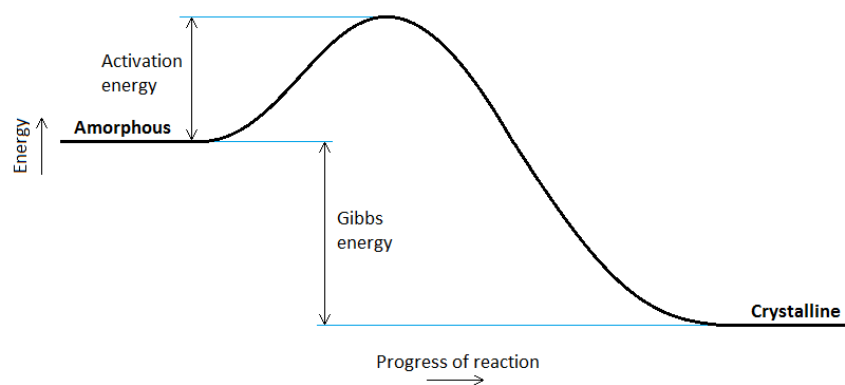


Figure 31: A schematic view of the exothermic reaction occurring from amorphous to crystalline. For crystallization, the material has to overcome an energy barrier (the activation energy). The Gibbs energy of the crystalline state is lower than the amorphous state, therefore energy is released which can be used to overcome the activation energy barrier during crystallization.

4.2.3 Isothermal measurements

As mentioned in the theory, isothermal measurements give a useful insight in the crystallization region. Both isothermal measurements were done with changing isothermal times and isothermal temperatures. However, because the evaporation of the samples was too large for higher isothermal temperatures, only the experiments with isothermal times provided useful data. Figure 32 shows the heating curves at 100 K/s after an isothermal measurement done at 150 °C for different isothermal times as was discussed in methods section 3.2 Figure 8.

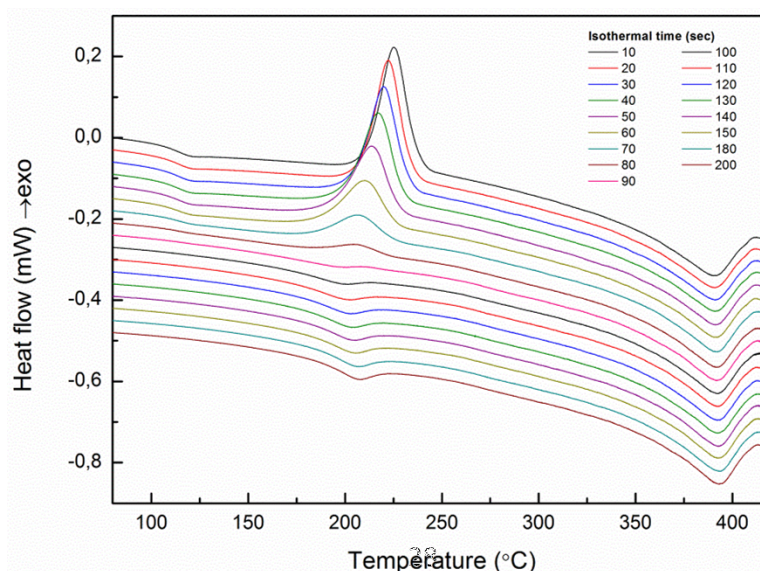


Figure 32: The heating curves after each isothermal segment for an isothermal temperature of 150 °C and different isothermal times including an offset in heat flow to prevent curves from overlapping too much. At the start of the measurement, the crystallization energy was 51 μJ and the melting temperature 341 °C (60%) which did not shift more than 2 °C during the measurements. Depending on the length of the isothermal segment, glass transition and crystallization are observed on subsequent heating or not at all. For the longest holding times a dip instead of a peak is observed at the crystallization temperature.

For low isothermal times there is not enough time to crystallize the sample, thus there is still a crystallization peak visible on the heating curve. At an isothermal time of 10 seconds the crystallization energy is comparable to the melting peak energy and crystallization energy after a melt-quench, thus the sample is still fully amorphous after the isothermal segment. As the isothermal time increases, the peak areas become smaller and eventually disappear. The peak temperature shifts to lower temperatures, which is due to the fact that the material is partly crystallized on the isothermal section, giving more seed crystals. Besides that, the glass transition also disappears simultaneously which indicates that the sample is fully crystallized. Due to the small change in heat capacity associated with the T_g , this is not further quantified. However, instead of the crystallization peak another endothermic transition appears at around 200 – 220 °C. For increasing isothermal times this transition starts appearing at higher temperatures. A possible explanation could be that the material is crystallizing in a different phase during the isotherms which reorganizes during the next heating curve. A longer isothermal time would result in a more stable crystal and therefore increases the temperature at which the crystal is then reorganized afterwards. Furthermore, the glass transition temperature of As_2Se_3 is also around 200 °C³⁸. Thus, it is possible that amorphous material of As_2Se_3 is formed at longer isothermal times which then gives rise to a glass transition at 200 – 220 °C. The shift in temperature could then be due to a change in composition of the amorphous phase. The crystallinity is obtained by measuring the area under the crystallization peak (Figure 33). Although the material still shows a glass transition, the crystallinity can be expressed as a percentage of the maximum possible crystallinity the material can achieve.

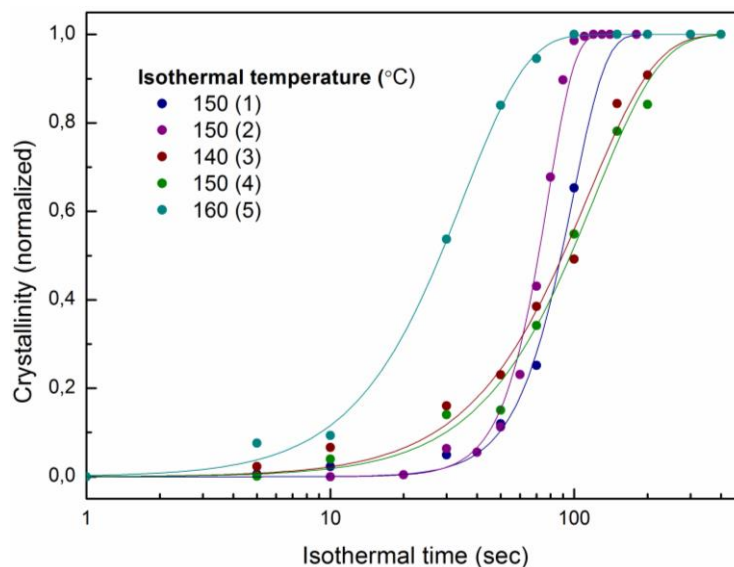


Figure 33: Isothermal S-curves which are fitted for several temperatures numbered by measurement. Measurement 1 and 2 were done on one sample and 3 till 5 on another sample. The curves show that at and below 150 °C, the order of time at which crystallization happens doesn't change much while for 160 °C it drastically lowers.

The figure shows that for isothermal temperatures of 140 and 150 °C, the time order at which the process occurs remains constant while at 160 °C it lowers drastically. For both samples the

parameters β and k and the samples composition, crystallization energy and isothermal temperature are given in Table 4.

Measurement	1	2	3	4	5
Composition Te/(Se + Te)*100%	57.3	59.9	54.3	53.4	51.6
Crystallization energy (μJ)	56.8	50.6	69.9	77.8	70.0
Isothermal temperature ($^{\circ}\text{C}$)	150	150	140	150	160
$\log(\beta)$	-6.4	-7.6	-3.2	-3.3	-2.6
k	3.2 ± 0.2	4.0 ± 0.5	1.6 ± 0.1	1.6 ± 0.1	1.7 ± 0.1

Table 4: The composition, crystallization, used isothermal temperature and fitting parameters for the isothermal measurements.

The k parameter for measurement 1 and 2 differs much ($\pm 20\%$) and is above 3 which indicate three dimensional growth. Measurement 3 till 5 which were done on another sample had a k parameter that varied slightly from 1.7. This allows anything between one and two dimensional growth depending on the value of n . Thus even though the crystallization energy, which is an indicator for the mass, and composition are within the same order of range for both samples, the growth can still be much different. The β is dependent on many other parameters and the data does not show any clear trends it is difficult to extract any physical meaning out of it. Research using isothermal segments was therefore not pursued past this point.

4.2.4 Discussion

The sample to sample variation of the Flash DSC experiments was large. An important reason for these variations is the sample size which significantly changed both the heating rates in the extended phase diagram and the activation energy. This was partly attributed to the crystallization that happens at the top of large samples which was observed using SEM in earlier research (and the absence of crystallization for smaller samples). To confirm this hypothesis, similar SEM images should be recorded for smaller samples. Another factor causing the variations is the heating contact between the sample and sensor. Previous research on SeTe showed that this did not significantly cause thermal lag for heating rates up to 1000 K/s. However, SeTeAs contains As which has a melting temperature above the Flash DSC limit and can therefore remain on the sensor when experiments are done.

The experiments have also shown that when SeTeAs crystallizes below 220 $^{\circ}\text{C}$, which was usually at lower heating rates, another transition occurred that decreased the heat capacity during crystallization and increased it back to its original value at higher temperatures. The isothermal measurements were also done at temperatures below 220 $^{\circ}\text{C}$ and they also showed a transition occurring at 200 – 220 $^{\circ}\text{C}$ when reheating. Because these transitions are also occurring at higher heating rates, it cannot be due an artefact of the Flash DSC at lower heating rates. It is yet unclear what kind of transitions are occurring, possible are a glass transition or reorganization of the crystal. Thus to gain more information about these transitions it is required to perform microscopy on these samples to investigate its structure.

4.3 Structure and thermal properties measured by DSC of SeTeSb

In previous research SeTe has been measured in the Flash DSC over a range of compositions to measure its phase changing properties. In this research a small amount of Sb was added to see how

this influences these properties. An ingot of $\text{Se}_{45}\text{Te}_{45}\text{Sb}_{10}$ was created by heating 3.55 g of Se, 5.74 g of Te and 1.22 g of Sb in vacuum in an oven at 650 °C for 8 hours. After that, the material was slowly cooled by convection to room temperature. An overview of the ingot can be seen in Figure 34.

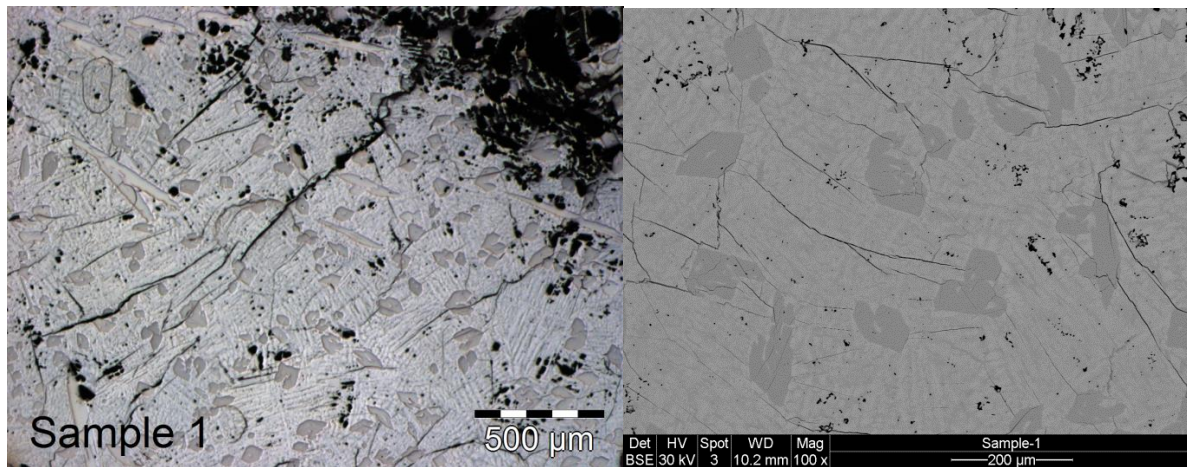


Figure 34: An overview of the SeTeSb ingot in the optical microscope (left) and in the SEM (right). Both images show grains in the size order of 50 to 100 μm . Furthermore, between the grains are lamellar structures visible.

The material shows large areas in the size order of 50 to 100 μm which have hexagonal or needle like shapes. Between these areas are lamellae oriented in the same direction which provide a similar microstructure as SeTe . The composition of these areas is measured with EDS which is shown in Figure 35 and Table 4.

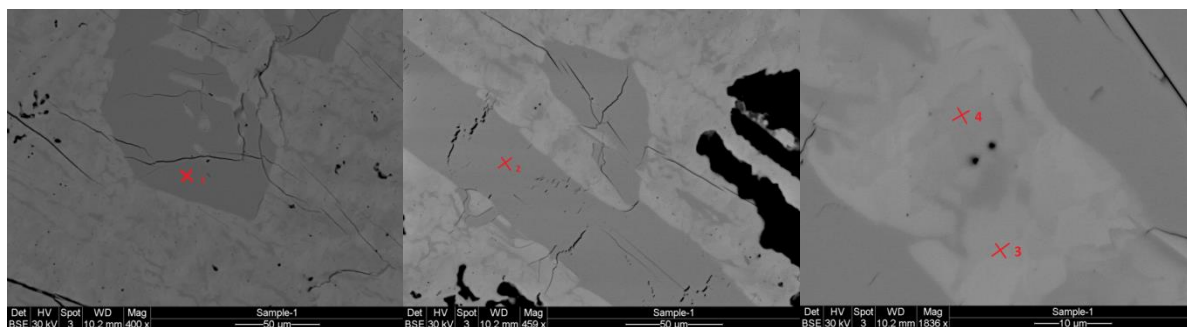


Figure 35: SEM images of the SeTeSb ingot which shows the spots that are measured with EDS.

Area	Se (at.%)	Te (at.%)	Sb (at.%)
Total	47.3	43.7	9.0
1 (hexagonal shaped)	60.4	0.4	39.1
2 (needle shaped)	60.1	0.4	39.5
3 (light)	35.7	63.1	1.3
4 (dark)	50.0	49.2	0.8

Table 5: Compositions of the areas measured with EDS in Figure 35 and the total composition.

The total composition of the ingot is within 2 at% to the target $\text{Se}_{45}\text{Te}_{45}\text{Sb}_{10}$ composition. The larger hexagonal and needle like grains contain about 60 at% Se and 40 at% Sb. According to the binary phase diagram of Se-Sb (Appendix A), these grains have the Se_3Sb_2 crystal structure which melts at a temperature of 590 °C. The other phase contains mostly Se and Te and a slight amount (< 2 at%) Sb. Although it will be impossible to melt the Se_3Sb_2 crystals in the Flash DSC, these crystals and the slight amount of Sb in the SeTe phase could still influence the phase change properties of the alloy. A

set of heating experiments is shown in Figure 36. The heating programme used was discussed in methods Figure 7 and similar to the one employed in studying SeTeAs in Figure 22.

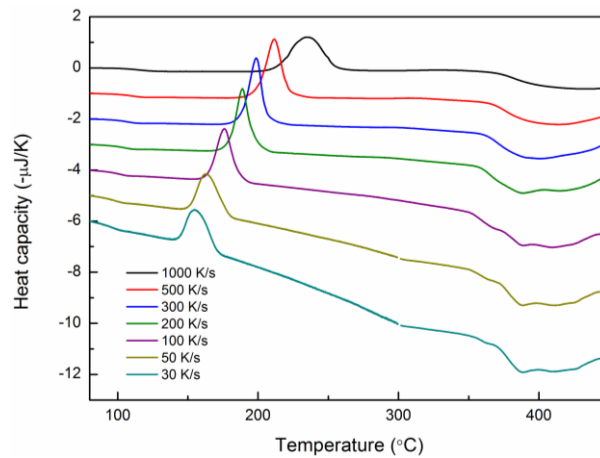


Figure 36: Several heating runs on SeTeSb for different heating rates. All data is normalized to the heating rate and an offset is present for clarity. Above all heating rates above 300 °C are changed to 100 K/s if they are lower than 100 K/s. This causes a large onset peak which is ~5 °C width which is omitted from the graph.

As can be seen, the glass transition lies at around 100 °C which is similar to SeTe and SeTeAs. Furthermore, the melting part has a well-defined onset like SeTe, but it does contain small subpeaks within the melting part itself, indicative of multi-phase melting. The glass transitions and crystallization rates can be put in an extended phase diagram as shown in Figure 37. Similar to the phase diagram of SeTeAs, the composition has been calculated by using a fit of the melting temperatures of the SeTe system.

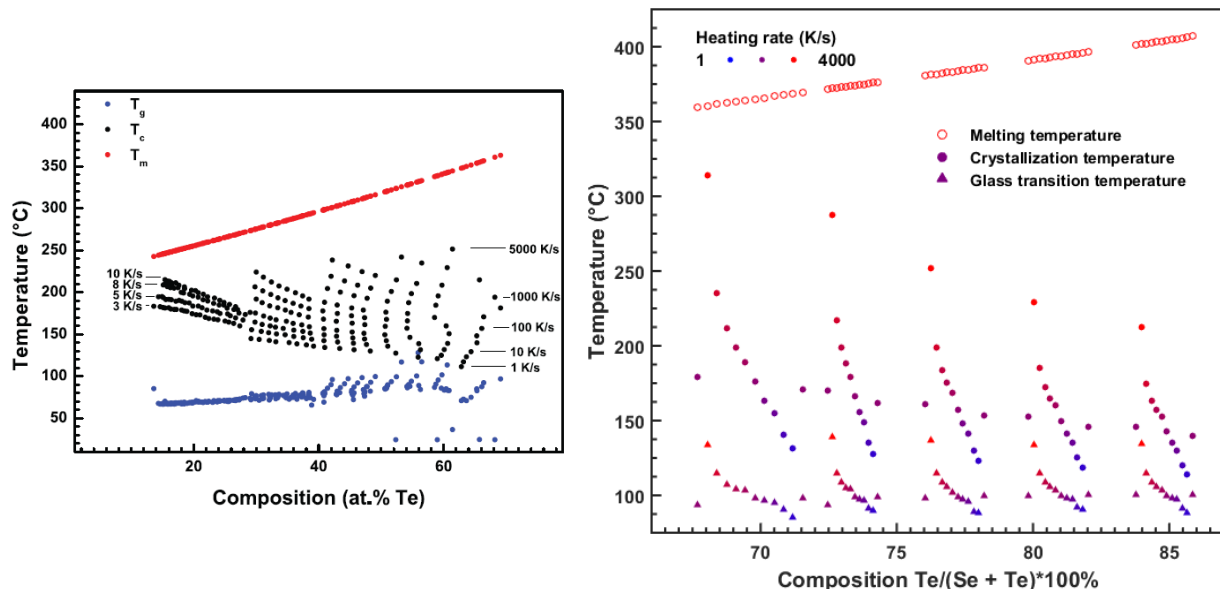


Figure 37: The extended phase diagram for SeTe (left) and SeTeSb (right) which shows the melting temperature and crystallization peak/glass transition temperatures for different heating rates. The melting temperatures for every measurement set have been linearly interpolated by using the measured melting temperatures. The glass transition and crystallization temperature continue to decrease for higher tellurium percentages. At 70% the crystallization temperature of SeTe and SeTeSb lie both at about 170 °C which is lower than the 230 °C for SeTeAs.²⁰

Although the glass transition is around the same temperature as the one of SeTeAs, the crystallization temperature is much lower (230 °C for SeTeAs compared to 170 °C for SeTeSb at 70 Te/(Se + Te)*100%). Two concurrent likely explanations for this could be that the As is a better glass

former which is segregated into the amorphous phase while the Sb is used to form Se_3Sb_2 which can act as nucleation site for crystallization. The reduced glass-transition temperature at 70% is 0.59 and at 85% it is 0.57. Therefore it is slightly lower than SeTeAs which indicates that SeTe with added antimony is a worse glass former than SeTe with added arsenic. At 70%, the glass transition temperature at a heating rate of 100 K/s of SeTe and SeTeSb is both around 100 °C. Also, at the same composition the crystallization temperature at a heating rate of 100 K/s is both about 170 °C. This indicates that the added antimony does not have much influence on the glass transition and crystallization temperatures. Kissinger analysis has been done on the crystallization temperature as shown in Figure 38.

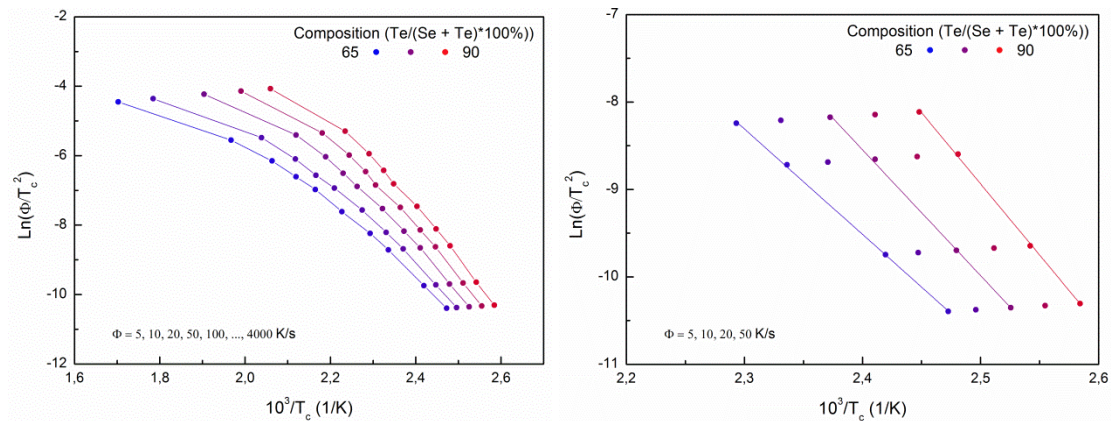


Figure 38: The Kissinger plot of the crystallization temperatures of SeTeSb (left). The Kissinger plot for heating rates below 100 K/s which is fit by linearly to measure the activation energy (right).

At higher heating rates the Kissinger plot shows a curvature which shows a non-Arrhenius behaviour consistent with the one for a fragile liquid. For low heating rates the slopes become relatively linear and the activation energy can be calculated, this is shown in Figure 39. The average composition of the data points in the Kissinger plot where used to obtain the composition for the activation energy.

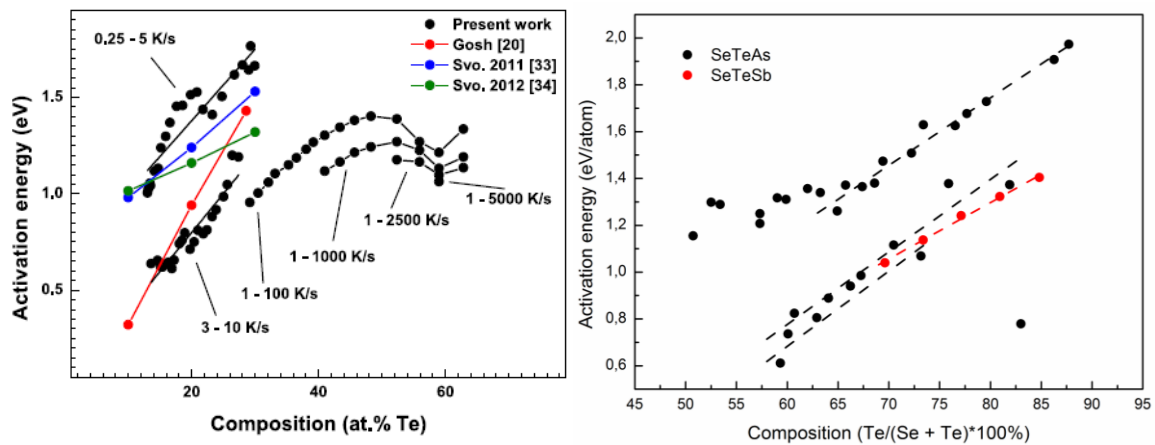


Figure 39: The activation energy of SeTe (left) and SeTeSb (right) for a range of compositions compared to the activation energies of SeTeAs. The activation energy of SeTeSb is similar to the samples with a lower crystallization energy for SeTeAs.²⁰

Similar to SeTe and SeTeAs, the activation energies increase when the ratio $\text{Te}/(\text{Se} + \text{Te})$ increases. The activation energies lies very close (< 0.2 eV) to the ones of the SeTeAs samples with a similar crystallization rate. Thus, it seems that even though the crystallization happens at different temperatures, the energy barrier for the growth process is similar. With a slope of 0.024 eV/at.%, the increase in activation energy with the composition is slightly smaller than the SeTeAs samples. A note

has to be taken that the composition shift is about 5% per heating run, this could result in an activation energy which is larger than the activation energy that would be obtained without compositional shift. Furthermore, the real composition of the material that was put in the Flash DSC is unknown. Since the crystals have a size in the order of 50 to 100 μm and the sample that is put in the Flash DSC is of the same size order of magnitude the composition can vary much from the total ingot.

4.4 Structure of (heat treated) SeTeAs

Although DSC measurements are able to give much information on phase transitions that are happening in a material, they do not provide all details to understand these processes. This is why it is often necessary to perform structural characterization like microscopy to determine what structural changes happen in the material during these transitions. To measure the structure and compositions on all length scales several types of microscopy and spectroscopy have been used: optical, SEM, TEM, EDS and STEM. By the use of these methods, the structure of heat treated SeTeAs is investigated.

The samples that were made by (ultrafast) DSC are shown in Table 6 including the type of microscopy that is performed on them. The samples from the Flash DSC had too small structures to be able to measure with optical microscopy or SEM, therefore they are only measured using TEM.

Material	Treatment	Heating rate (K/s)	Optical	SEM	TEM
Se ₄₅ Te ₄₅ As ₁₀	Ingot	-	x	x	x
Se ₄₅ Te ₄₅ As ₁₀	DSC	0.5	x	x	
Se ₄₅ Te ₄₅ As ₁₀	Flash DSC	5			x
Se ₄₅ Te ₄₅ As ₁₀	Flash DSC	100			x
Se ₄₅ Te ₄₅ As ₁₀	Flash DSC	-100			x

Table 6: The samples of SeTeAs that were investigated including their treatment, heating rate at which they were crystallized and the types of microscopy applied to them.

The ingot samples were made by slowly cooling the material in an oven from the melt which takes at least 8 hours. The DSC sample was crystallized with a heating run up to 300 °C by using the heating scheme described in the method section, the heat flow of this sample is shown in Figure 40.

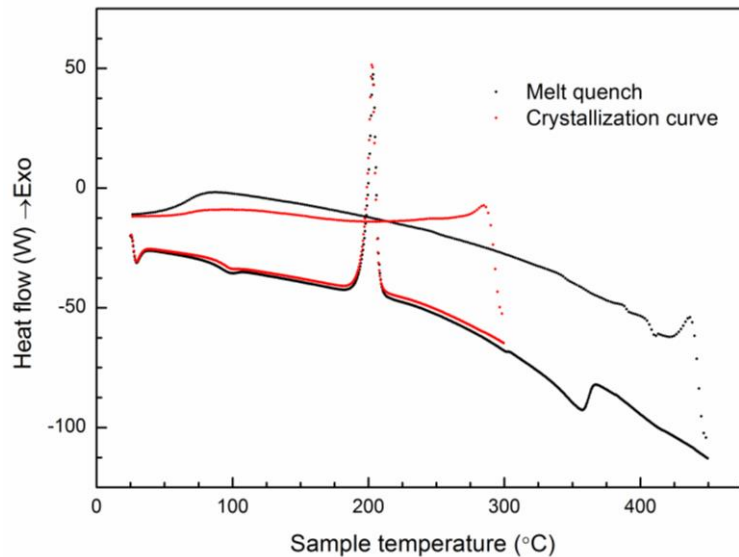


Figure 40: DSC measurements done on a SeTeAs sample to crystallize it at a heating rate of 100 °C/min. After the sample is crystallized on the crystallization curve there is still a small glass transition visible on the cooling. This is however not as pronounced as the glass transition on the cooling curve of the melt quench.

The crystallization peak temperature of the DSC curve is 203 °C and the melting onset is 300 °C. On the cooling curve of the melt quench there is only a glass transition visible indicating that the material has become fully amorphous. After the sample has crystallized there is a significant smaller glass transition visible on the cooling curve. This means that not all of the amorphous material has been crystallized, thus there is still amorphous material present.

Furthermore, four samples of SeTeAs were made in the Flash DSC using the heating scheme described in the method section. One sample was made by cooling from the melt. Three of the samples were crystallized by heating them from the amorphous phase: one with 5 K/s to 270 °C, one with 100 K/s to 240 °C and one with 100 K/s to 260 °C.

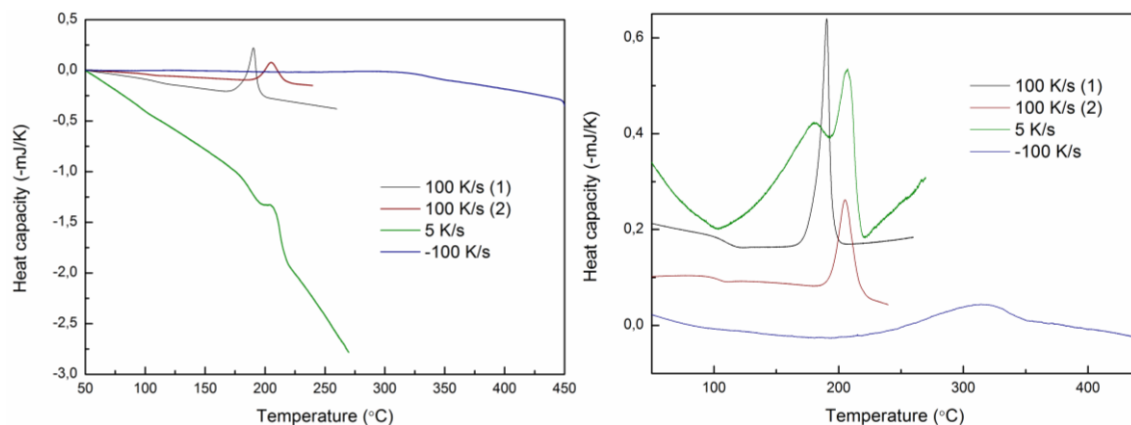


Figure 41: The Flash DSC curves which show the crystallization for several samples that are turned into TEM samples (left) and the curves with a subtracted quadratic fit made with the least square method (right). Three samples are crystallized on the heating run and one on the cooling run. The crystallization peak on the cooling curve is broader and occurs at a higher temperature than the crystallization peaks on the heating curve.

As can be seen, both samples that crystallized at 100 K/s had a different crystallization temperature. This can be due to either the difference in composition, size of the samples or the thermal contact. Although the 5 K/s peak is as broad as the 100 K/s, the time it takes is longer thus the crystallization process takes slower than the 100 K/s heated samples. The crystallization peak of the cooled sample is much higher in temperature due to the fact that it crystallized from the melt. It is also about 3

times as broad in temperature range as the samples that were crystallized during the heating process. The glass transition, crystallization temperature and melting temperature of the melt quench are given in Table 7 to compare the initial state of the samples. Furthermore, the crystallization temperature, energy and peak width are given.

Treatment	Melt quench			Crystallization run			TEM-EDS
	T _c at 100 K/s (°C)	T _m at 100 K/s (°C)	Composition (at.% Te/(Se + Te))	T _c (°C)	E _c (10 ⁻³ mJ)	Crystallization peak width (°C)	Composition (at.% Te/(Se + Te))
5 K/s	328	359	68	208	33	~30	57
100 K/s (1)	190	353	64	190	45	~40	55
100 K/s (2)	208	335	51	205	28	~40	54
-100 K/s	316	355	64	309	25	~120	54

Table 7: The crystallization temperature, melting temperature and composition inferred from the melting temperature are given of the melt quench; this is done to compare the initial state of the samples. The crystallization temperature, energy and the width of the crystallization peak are given for the heating run at which the sample crystallized. Finally, the composition measured by TEM-EDS, discussed later on, is added.

While the compositions measured by TEM-EDS are all within a few degrees from each other, the composition inferred from the melting temperature is definitely not. This is due to the long onset of the melting trajectory of SeTeAs which makes the determination of the melting onset difficult. Furthermore, the crystallization temperature of the sample crystallized at -100 K/s is about 100 °C higher than the other samples and about 3 times broader. This is due to the fact that this sample is crystallized from the melt while the others are crystallized from an undercooled liquid.

4.4.1 Microstructure overview

The ingot and DSC sample both contained enough material to measure the structure at milli and microscale. These samples are made by using the method described in the method section 3.2, optical microscopy images are shown in Figure 42.

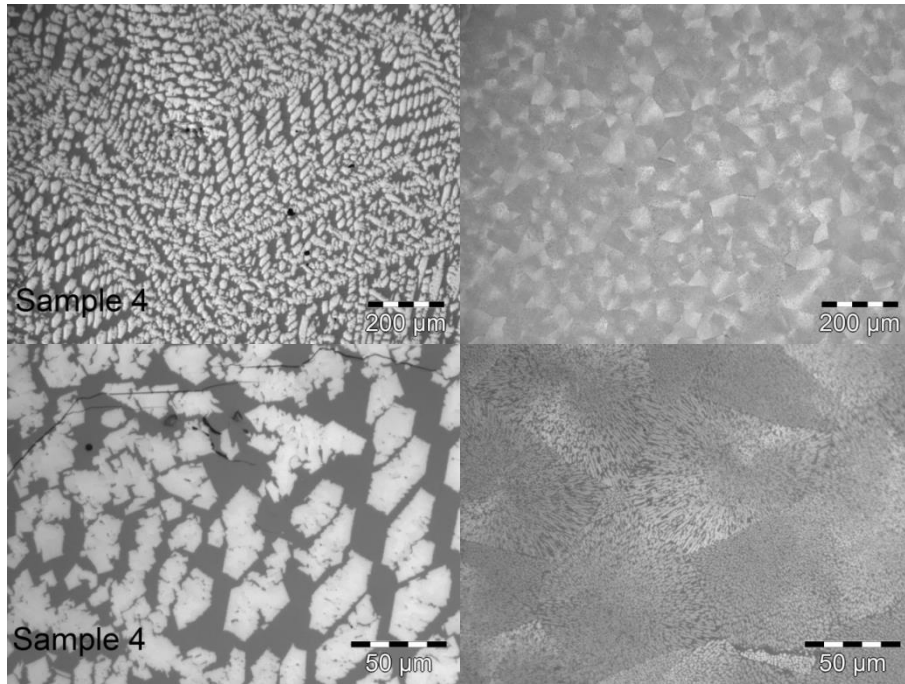


Figure 42: Optical reflection image of the ingot sample (left) and DSC sample (right). The ingot shows crystals in the size order of $10\ \mu\text{m}$ surrounded by amorphous material. The DSC sample shows much smaller crystals that are ordered in a spherulitic structure which has a size in the order of $50\ \mu\text{m}$.

As can be seen, the ingot contains highly reflective large crystals with a length in the size order of $10\ \mu\text{m}$ which are surrounded by a less reflective matrix. These crystals seem to be lying in domains that have an ordered structure on the submillimeter scale. The DSC sample contains much smaller crystals which are grown with a spherulitic structure and which have a length of about $50\ \mu\text{m}$. Again a phase separation is observed. Smaller scale optical and SEM images are shown in Figure 43. These show a clear difference in the ingot crystals which contain sharp boundaries and are hexagonally shaped while the crystals from the DSC are much more rounded crystals. The crystals from the DSC are smaller in the center of the spherulites and become longer and needle like near the edge.

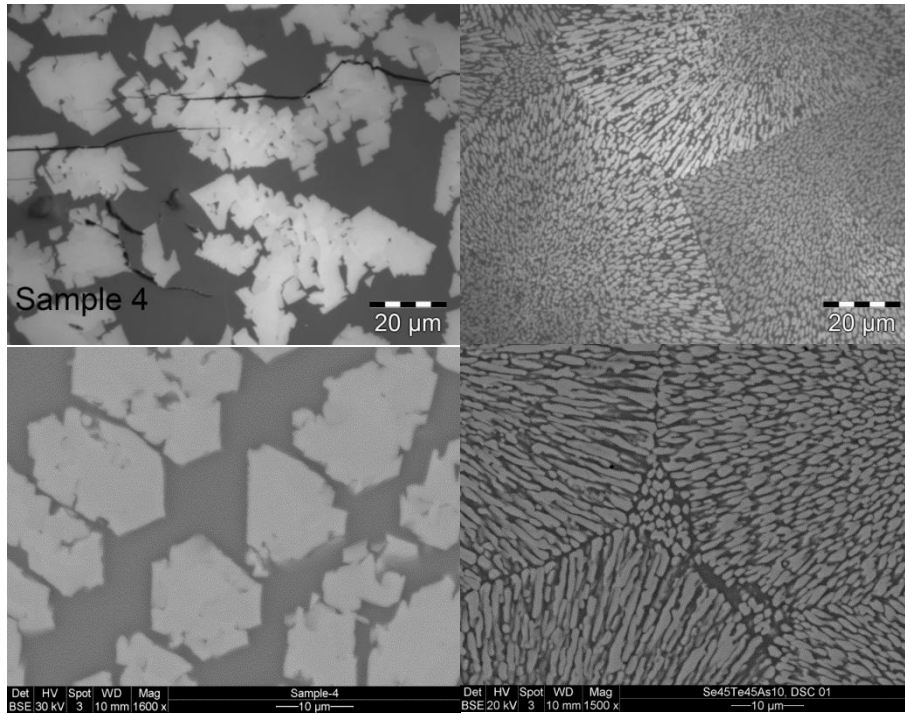


Figure 43: Optical (top) and SEM (bottom) overviews of the ingot sample (left) and DSC sample (right). The crystals in the DSC sample are smaller in the centre of the spherulites and get longer near the edges.

The crystallinity can be calculated by setting a threshold for the intensity in the pictures and then count the ratio between black and white pixels (Appendix B). This is done for both samples and the result is shown in Table 8. The difference in crystallinity is only 3% for the DSC sample and the ingot. Furthermore, the average crystal diameter is calculated by using a threshold on the picture followed by an algorithm to connect the grain boundaries to calculate the average crystal diameter (Appendix B).

Treatment	Crystallinity (vol %) (image)	Average crystal diameter (µm)
Ingot	58.0	17.7
DSC	61.3	1.7

Table 8: The crystallinity is determined by using a threshold on the image, by the composition and the average crystal diameter. While the crystallinity is similar, the average crystal diameter is about 10 times higher for the ingot sample.

As can be seen, both the overall crystallinity and the composition of the samples are similar. However, the average crystal diameter is a factor 10 smaller for the DSC sample. The composition of the samples is measured by SEM-EDS. This is done for the total composition and for the crystal phase (light) and amorphous phase (dark) which is shown in Table 9. It has to be noted that the SEM-EDS probe has a large interaction volume (diameter typically 1 µm) compared to the size of the structures which is in the order of 2 µm. Since the DSC sample contains structures that are smaller or equal than this probe, it is likely that the error of the composition is larger due to the overlap.

Treatment	Area	Se at.%	Te at.%	As at.%
Ingot	Total	49.3	40.2	10.6
	Crystalline	33.7	63.5	2.8
	Amorphous	63.3	15.6	21.1
DSC	Total	48.8	41.4	9.8
	Crystalline	41.0	54.9	4.1

	Amorphous	60.3	22.0	17.7
--	-----------	------	------	------

Table 9: Composition of the ingot and DSC sample measured with SEM-EDS. The composition is similar for the ingot and DSC sample. The crystalline regions contain more tellurium while the amorphous regions contain more selenium and arsenic.

The total composition of the ingot and DSC sample contained slightly more selenium and slightly less tellurium (5 at%) than the intended $\text{Se}_{45}\text{Te}_{45}\text{As}_{10}$ material. Since the DSC sample is made from the ingot material, it can be concluded that the DSC treatment did not have any influence on the composition. The crystal phase contains more tellurium and less arsenic than the amorphous phase for both the ingot and the DSC sample. For the DSC sample this difference is less which could be due to the fact that the probe had an overlap on the structures as explained earlier, or due to the higher rate of crystallization, which might prevent full demixing.

For the 100 K/s heated sample it was not possible to obtain a good optical microscopy image (Figure 44 left). This is due to two reasons: one is because the structures were too small to be distinguished in the optical microscope and the other is because the optical working distance was too small to tilt the sample into focus due to the sample being obstructed by the ring that supports it. This former problem does not hold for the SEM and it is also possible to image at much smaller length scales as shown in Figure 44 right. However, the structures within the sample are still too small to get quantitative information about the structure. Therefore, it is necessary to perform measurements in the TEM to find more about the structure of the samples that are treated in the Flash DSC.

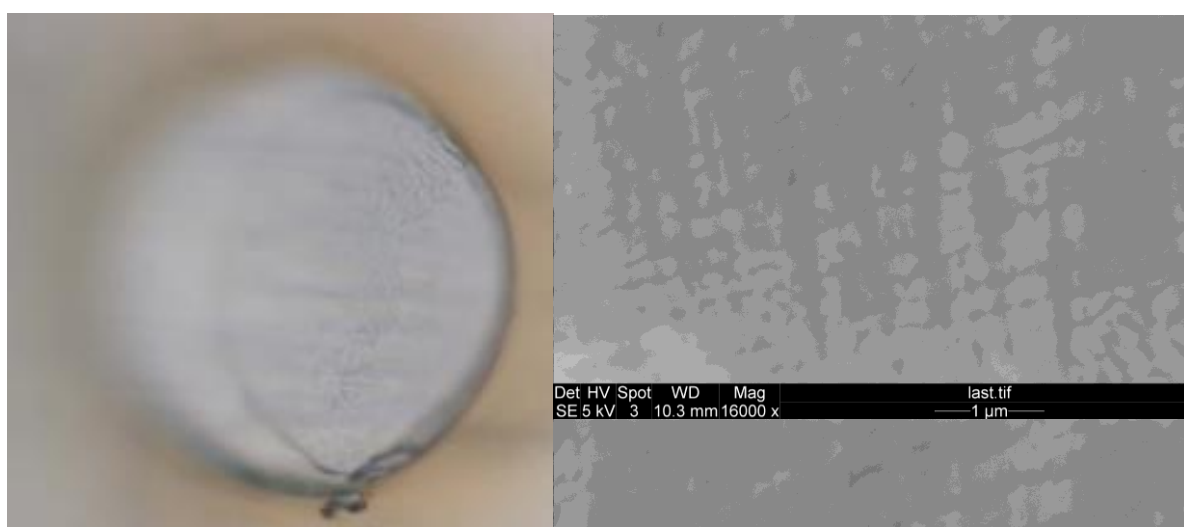


Figure 44: Optical measurements that were done on 100 K/s heated SeTeAs which was measured in the Flash DSC (left). The lamellae are slightly visible but it was not possible to tilt the whole sample into focus due to a too short optical distance. The SEM measurements (right) also showed lamellae, but these were also too small to obtain more qualitative data like SEM-EDS spectra.

4.4.2 Nanostructure overview

All the samples except the DSC sample have been investigated with TEM to obtain the structure at nanoscale. Overview images of the ingot, 5 K/s, 100 K/s and -100 K/s heated samples are shown in Figure 45.

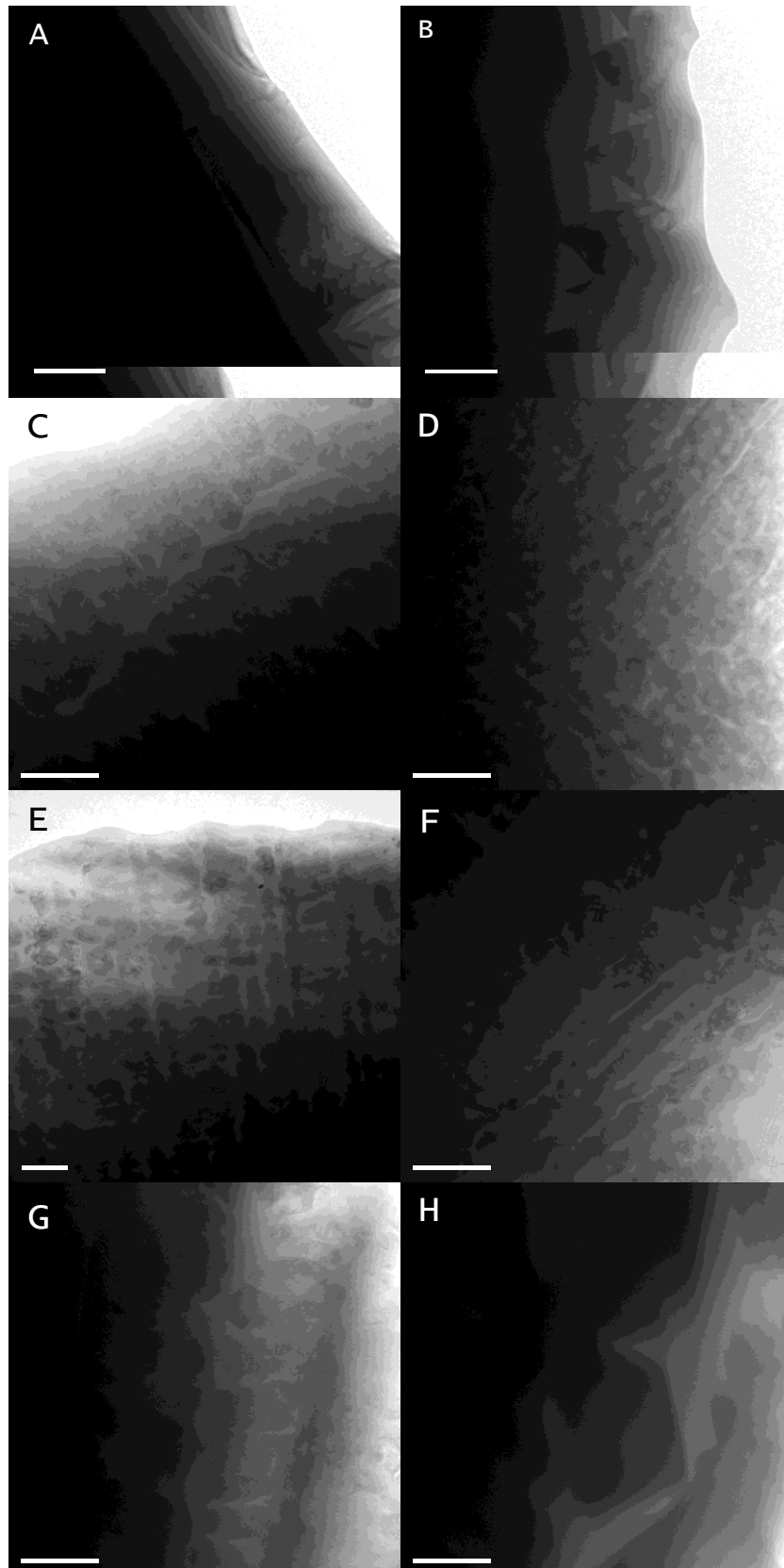


Figure 45: TEM overviews of the ingot (a/b), the 5 K/s heated sample (c/d), the 100 K/s heated samples (e/f) and the 100 K/s cooled sample (g/h). The ingot sample contains large crystals with sharp boundaries. In the other samples, lamellae are visible of which some contain side chains. In the 100 K/s cooled sample the crystal structures are larger than the 5 K/s and 100 K/s heated samples. Since the 100 K/s heated samples had the same structure, they are treated as one sample further on unless told otherwise.

The structure of the 100 K/s heated samples turned out to be equal, therefore they are treated as one sample in the further sections unless told otherwise. Like the DSC sample, the samples treated in the Flash DSC show a lamellar growth structure. The TEM does not provide a large enough overview to see spherulites. However, for the 5 K/s and 100 K/s heated samples there are boundaries visible between the lamellae which indicate a boundary between two spherulites (Figure 45c/d/f). Also the lamellae in these pictures are not completely parallel but have a slight angle which indicates that they are grown outward in spherulite structures. The 100 K/s heated and cooled samples also contain side branches which have a 90 degree angle compared to the main lamellae (Figure 45e/g). Furthermore, the 100 K/s cooled sample also contains larger individual crystals similar to the ingot sample (Figure 45h).

Treatment	Crystallinity (vol %)	Crystallinity (at %)	Average crystal diameter (μm)	Lamella thickness (μm)
Ingot	58.0	50.8	25.0	-
1 K/s (DSC)	61.3	59.0	2.5	0.80 – 1.30
5 K/s	-	-	-	0.12 – 0.26
100 K/s	-	-	-	0.12 – 0.20
-100 K/s	-	-	-	0.25 – 0.40

Table 10: The crystallinity, average crystal diameter and lamellae thickness for the samples compared to each other. The size of the lamella of the Flash DSC heated samples are very similar while the lamella in the DSC heated sample are about ten times larger.

The crystallinity and size of the structures is shown in Table 10. A circle has been constructed with a surface equal to the average crystal surface. The diameter of this circle (called average crystal diameter) is then calculated to give an indication of the size order of the crystals:

$$d = 2 \sqrt{\frac{A}{\pi N}} \quad (5)$$

where A is the total crystallized area and N the amount of crystals counted. The average crystal diameter gives an indication of what size order the crystals are. However, since the sample created with the (Flash) DSC contains lamellae instead of spherical crystals the lamella thickness is also given to give an indication of the size of these structures. The lamellae thickness has been estimated by measuring them in the image; the minimum and maximum thickness' that are found are stated. As can be seen, the size of the structures of the cooled sample is larger than the size of the heated Flash DSC samples. Again, the reason for this is likely that the atoms are more diffusive when coming from the melt and thus the material is able to segregate the arsenic and selenium to the amorphous phase more easily. The difference for the 5 K/s and 100 K/s heated samples in the Flash DSC is not very large in terms of structure and size. However, the difference between the 1 K/s heated DSC sample and these samples is much larger. The reason for this could be that in the DSC the sample was quenched at a much smaller cooling rate and that the sample environment was different, as described in methods section.

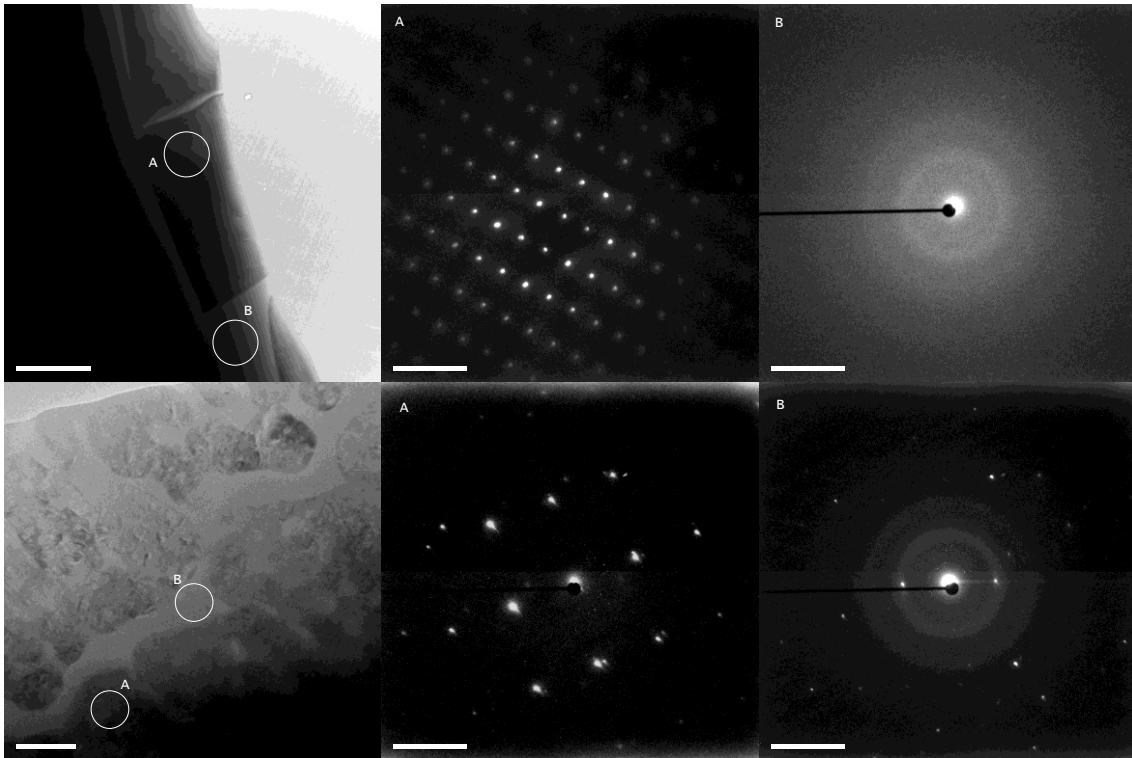


Figure 46: Diffraction patterns of the ingot (top) and the 5 K/s heated sample (bottom) showing that the material contains both crystalline and amorphous phases. In diffraction pattern B for the 5 K/s heated sample there are still diffraction spots visible since the diffraction aperture had some overlap with the crystals around the amorphous phase.

Diffraction has been performed to confirm that the material consists of both amorphous and crystalline areas. This is done for the ingot and the 5 K/s heated sample (Figure 46). The diffraction patterns show only spots and no amorphous ring in the dark areas while the light areas show amorphous rings. The diffraction pattern of the amorphous region in the 5 K/s heated sample also shows diffraction spots, these are however due to the fact that the aperture size is too large and contains some crystal material around the amorphous area.

4.4.3 Composition

The composition of the samples was measured by using EDS and STEM. STEM has been performed on the ingot sample and the 100 K/s heated sample to obtain elemental maps and line scans. Figure 47 shows the elemental maps of crystalline and amorphous phases in the samples. In the bright field images, the crystals show up as dark area while the amorphous shows up as light area. From the spectral data it becomes clear that for both samples the amorphous phase contains more As and Se while the crystalline phase contains more Te. Since the size of the STEM probe is unknown, it is not possible to tell whether the gradients in composition that are shown are due to the probe size or due to a compositional gradient in the material.

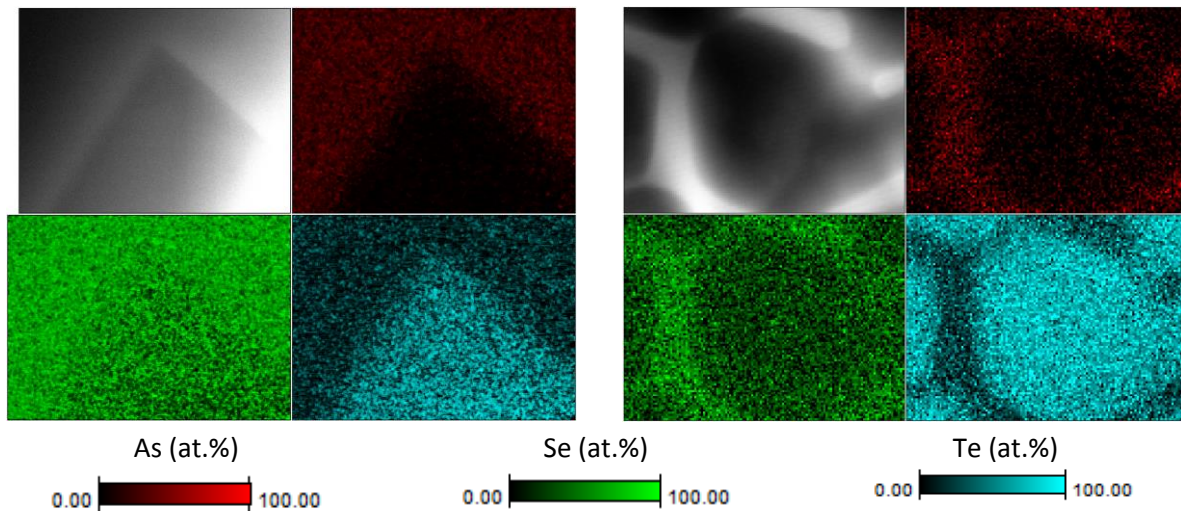


Figure 47: Spectral images of the ingot (left) and the 100 K/s heated sample (right) including the electron image. The composition of As is shown in red, Se in green and Te in blue for the ingot. For the 100 K/s heated sample As is in blue, Te in green and Se in red. The scale of the left image is in the order of micrometers while the right image is in the order of 10's of nanometers. Both images show that the arsenic is mostly in the amorphous region and the tellurium mostly in the crystalline region. The selenium concentration is found in both regions but the concentration in the amorphous phase is larger.

Line scans have been performed on the same areas to show how the composition changes in the material (Figure 48). For the ingot, a line scan was performed in two directions perpendicular to each other. As can be seen, the composition is constant throughout the whole crystal within a margin of 5 at.%. In the line scan for the 100 K/s heated sample it can be seen that the composition in the amorphous phase was not uniform. The thickness of the amorphous/crystalline boundary is measured to be 1 nm or less thick (see section 4.4.4). Because the onset and offset of the linescans are similar, it is assumed that there is no significant composition gradient near the amorphous/crystalline boundary. Thus, it is assumed that the onset and offset are due to the probe size. The probe size is then equal to the onset plus offset of the composition gradient, which is in the case of the ingot in the order of 200 nm.

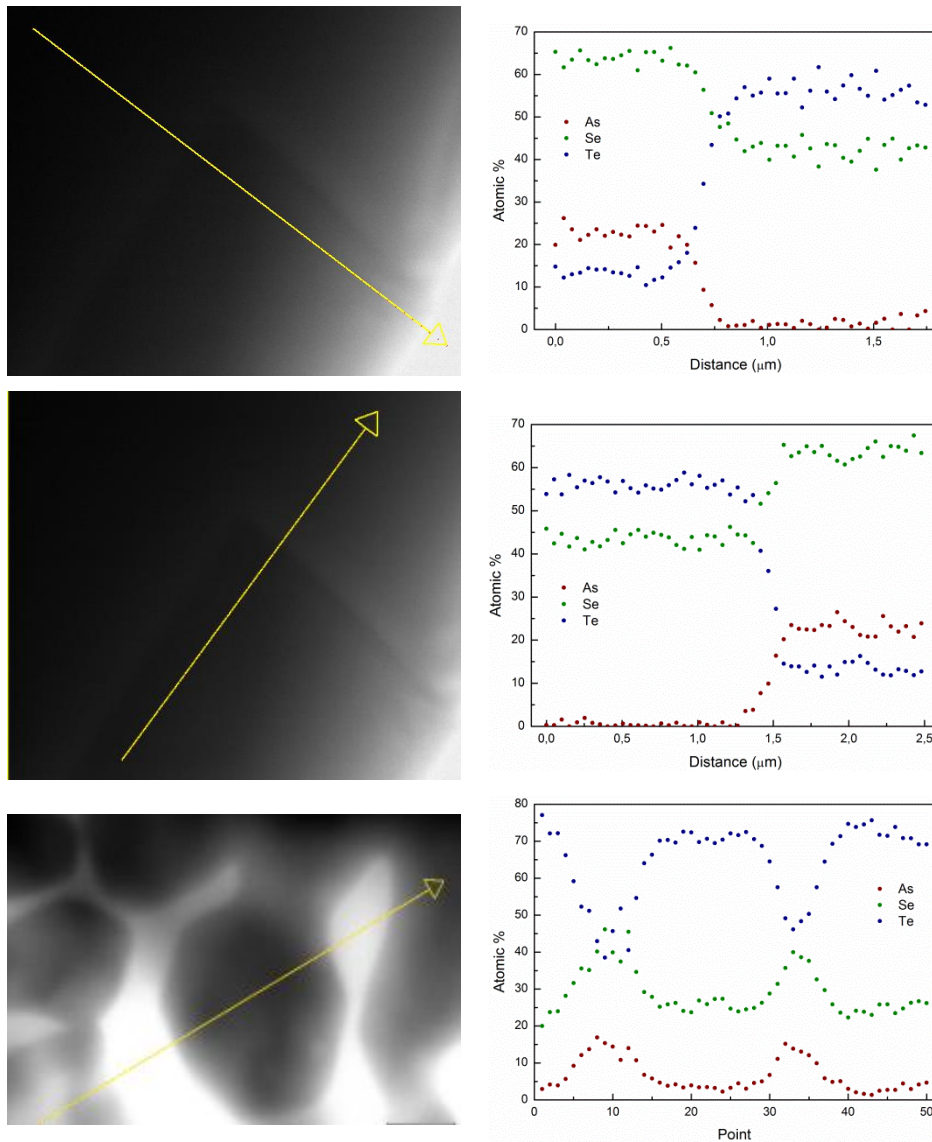


Figure 48: Linescans made by STEM on the ingot (top/middle) and the 100 K/s heated sample (bottom). It is clear the crystalline areas contain more Te and less Se and As than the amorphous phase. Due to the convolution of the probe and boundary, boundary thickness cannot be easily obtained. The linescans show that the concentration in amorphous and crystalline phase doesn't vary significantly (< 5 at%).

The total composition of all samples has been measured by EDS except for the ingot (Figure 49). The composition of the ingot is taken from the SEM-EDS data because the structures were too large to obtain a representative overview by TEM-EDS. For every sample 3 to 7 areas were analysed with a selected area aperture corresponding to a sample area with diameter of about 2 μm. The averaged results are shown in Figure 49 and the individual data can be found in Appendix D.

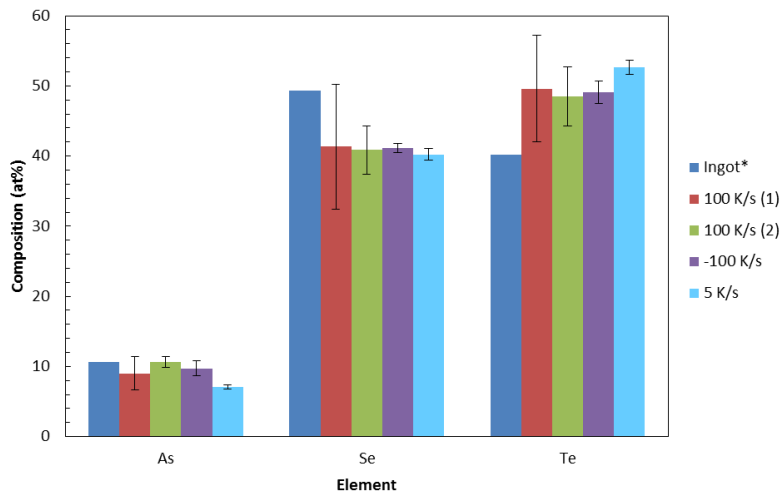


Figure 49: The average composition of the samples measured by EDS for several overviews. The Flash DSC treated samples all have a similar composition while compared to the ingot, their selenium percentage is about 15 – 20% lower and their tellurium percentage is about 15 – 20% higher. Furthermore, the composition of both 100 K/s is also similar (< 2 at.% variation).

All samples treated in the Flash DSC have about 15 - 20 at.% less selenium than the ingot and 15 – 20 at.% more tellurium. This indicates that, even though not many measurements were done on the sample, there is still a significant amount of evaporation of selenium during the Flash DSC measurements. The error bars show the standard deviation for different measurements within the material; it can be seen that the variation in the 100 K/s heated samples is larger than the others. The composition of the 100 K/s heated samples deviates less than 2 at.%. However, the error bars of both samples are larger than 5 at.% which is due to the variation in composition through the material.

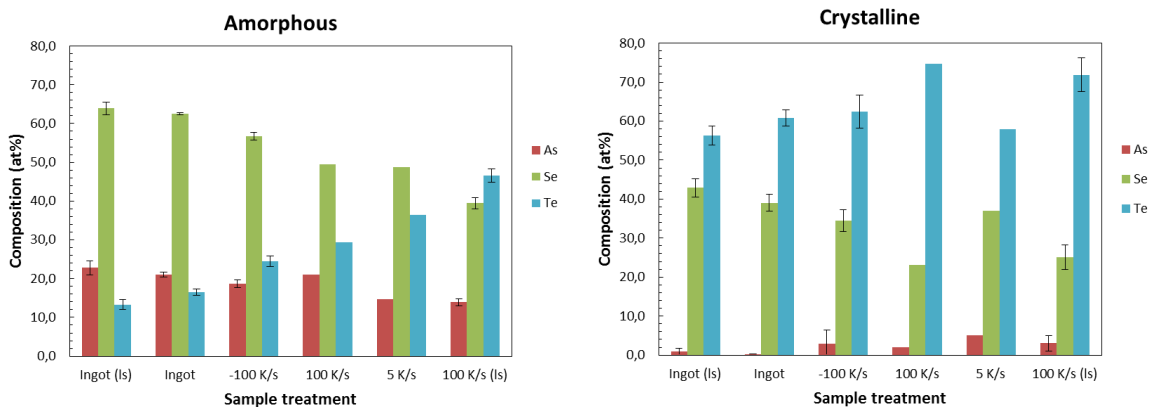


Figure 50: The average composition for the amorphous phase (left) and the crystalline phase (right). For the ingot and 100 K/s heated sample the composition is measured with EDS and with an average of a linescan. All samples show that most of the arsenic (15 – 25%) is found in the amorphous phase. The difference in selenium and tellurium is largest for the ingot samples for the amorphous phase.

Figure 50 shows the composition that is measured in both crystal and amorphous phase. The minimum achievable spot size was around 200 nm. Thus, this was used to probe the crystal and amorphous regions. Since the lamellae are in the same order of length and most of the amorphous material is even smaller, it could be that the probe overlapped both crystalline and amorphous phases. This would result in the composition of the amorphous and crystalline material being more equal to the total composition. However, this effect is minor and there is still a clear difference for

both phases. The amorphous material contains 15 to 20 at% As for all samples while the crystalline material contains hardly any As. Also, the crystalline phase contains 20 to 50 at% more tellurium than selenium while the amorphous phase contains 10 to 50 at% more selenium than tellurium. This is consistent with the fact that selenium and arsenic are good glass formers while tellurium is not. The sample that is cooled with -100 K/s has a composition that is closest to the ingot. This is likely due to that it is also crystallized by cooling from the melt while the other samples are crystallized by heating from the amorphous phase. It is not possible yet to quantify differences between the heated samples since there are not enough measurements done to give accurate statistics.

4.4.4 Atomic structure

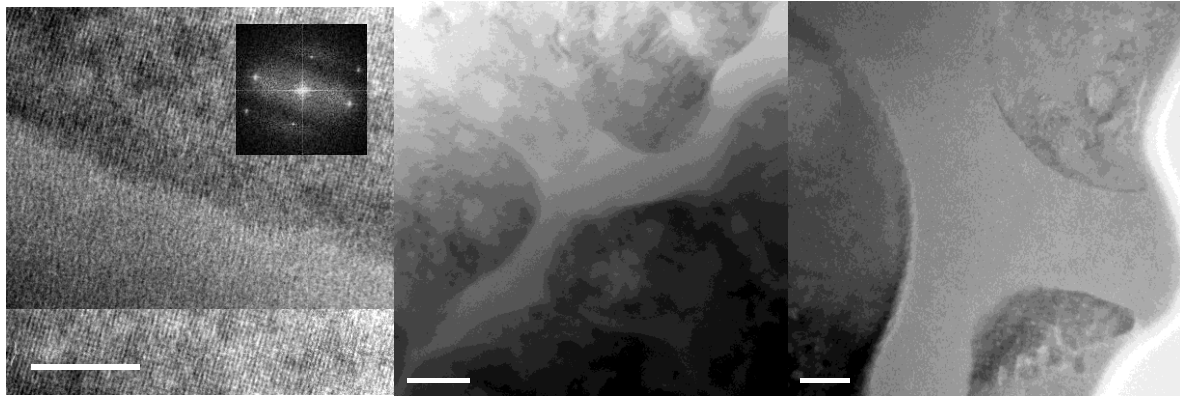


Figure 51: Zoom in on the boundary between the amorphous/crystalline phase for the ingot (left), the 5 K/s heated sample (middle) and 100 K/s heated sample (right). The inset shown in the left image shows the FFT of the image of the ingot. The images show there is a sharp boundary between the amorphous and crystalline phase.

Higher magnification images are shown in Figure 51 of the ingot, 5 K/s and 100 K/s heated samples. The ingot contained larger crystals which made it possible to capture atomic resolution images. This shows clearly that there is a sharp boundary between the crystal and amorphous phase. Although atomic resolution images of the 5 and 100 K/s heated samples were not obtained, their images still show that the crystals also possess sharp boundaries which are less than 1 nm thick.

From all the diffraction patterns, the atomic structure can be determined. As mentioned in the theory, selenium, tellurium and arsenic have structures belonging to the trigonal crystal system. All the diffraction patterns contain spots that are in agreement with this crystal type, thus it is assumed that the $\text{Se}_{45}\text{Te}_{45}\text{As}_{10}$ has the same structure but different lattice parameters. The lattice parameters a and c were calculated from the diffraction pattern by using the spots of the lowest hkl planes which are the $\{0\ 0\ 1\}$, $\{0\ 1\ 0\}$, $\{0\ 1\ 1\}$ and the $\{1\ 0\ 1\}$ reflections. It was also possible to measure the lattice parameters of the ingot by using FFT on high resolution images. The averages of these lattice parameters are shown Figure 52. Besides that, the theoretical value a and c are calculated based on Vegard's law and are shown as well in Figure 52.

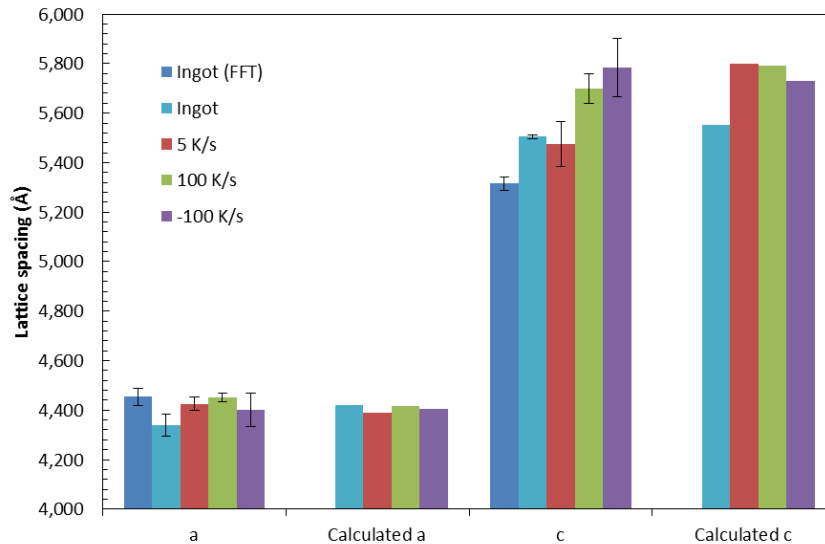
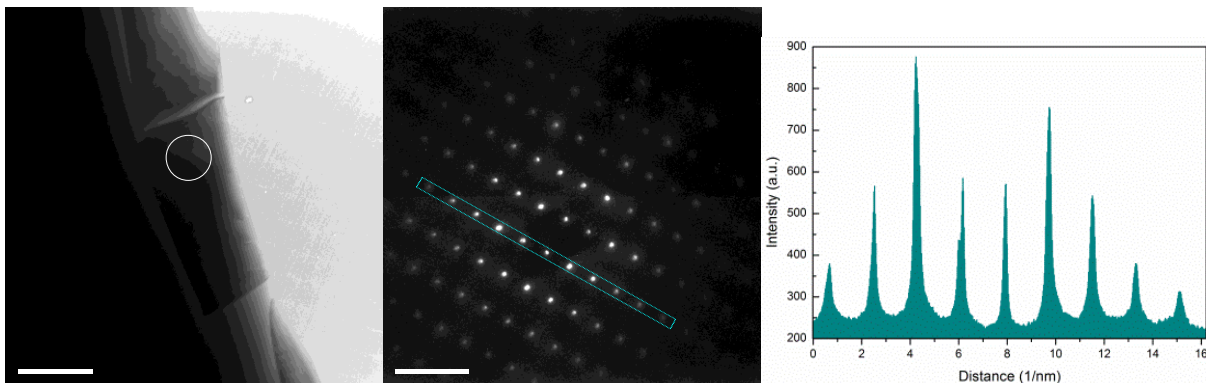


Figure 52: Lattice parameters a and c that are measured from diffraction patterns and their theoretical values based on the composition for the different samples. Also shown are the lattice parameters a and c that were calculated based on the FFT of high resolution images. The difference between the lattice parameters inferred by FFT and diffraction images is due to a misalignment in the FFT. The other lattice parameters are consistent with their theoretical value from Vegard's law, thus the differences in lattice parameters are mostly due to composition.

The lattice parameters measured by diffraction and FFT for the ingot sample seem to be 0.2 \AA off. An explanation for this offset is that the calibration of one of these methods is incorrect. If both diffraction patterns and FFT images are taken at this error in calibration wouldn't show up; the FFT patterns, however, are all taken at the same orientation. Since the lattice parameters inferred of the diffraction patterns are reasonably consistent with the theoretical value by Vegard's law, it is assumed that the FFT had a misalignment. The other lattice parameters are very similar to each other for each sample (differences $< 0.2 \text{ \AA}$). The difference can be due to the fact there is also a variation in composition for different crystals within the samples. Especially the lattice parameter c of for arsenic (10.548 \AA) is much larger than selenium (4.368 \AA) and tellurium (4.454 \AA). Thus, when there is more arsenic present, it will increase the c parameter for the crystal. This is also shown by the theoretical values. However, only for the 5 K/s sample the theoretical and calculated values for the c parameter do not agree. Of course Vegard's law is also a simplistic model to calculate alloy lattice parameters, and as such we find that the experimental data agrees well with the predictions of the model.

For pure selenium or tellurium the $\{0\ 0\ n\}$ and $\{0\ 0\ 2n\}$ reflections are forbidden due to the $P_{3_1} 2 1$ symmetry. This structure has a threefold screw symmetry along the c axis which causes the periodicity to be three times larger along the c axis than a trigonal structure without such screw axis.



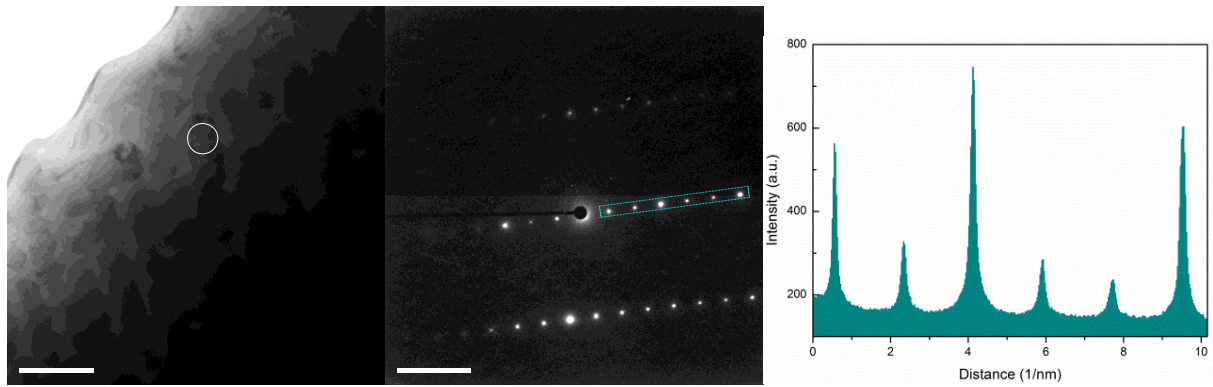


Figure 53: Diffraction on the ingot (top) and 100 K/s heated sample (bottom) showing the intensity for the $\{0\ 0\ n\}$ peaks. The intensity profile of the boxes in the diffraction patterns are shown in the length. For the ingot the central peak lies at $4.2\ \text{nm}^{-1}$ while for the 100 K/s heated sample it is blocked and therefore not shown. Both samples show that the intensities of the $\{0\ 0\ 3n\}$ peaks are larger which indicate that the structure possesses a $P\ 3_1\ 2\ 1$ symmetry.

Figure 53 shows two diffraction patterns of $\{0\ 0\ 1\}$ peaks and its intensity profile. Both diffraction patterns are taken close to a zone axis. However, as can be seen in the diffraction images the $\{0\ 0\ n\}$ and $\{0\ 0\ 2n\}$ planes are still reflecting, although not as much as the $\{0\ 0\ 3n\}$ planes. The intensity of these peaks can be calculated with the structure factor as shown in Appendix C. Because the $\{0\ 0\ 3n\}$ peaks are more intense than the $\{0\ 0\ 2n+1\}$ and $\{0\ 0\ 2n + 2\}$ peaks, it is concluded that the SeTeAs structure also possesses a $P\ 3_1\ 2\ 1$ symmetry. Furthermore, there are no diffraction spots found that indicate a superlattice, thus it is assumed that the Se, Te and As are ordered randomly.

Since the atomic structure is known, the growth direction of the lamellae can be determined by combining diffraction patterns and images. These lamellae are shown for the 100 K/s heated sample in Figure 54 and their orientation are indicated by red lines. Since the lamellae slightly diverge during outward growth due to the spherulitic structure, there is a small angle between their orientations. The orientations which have the largest angle between them are shown in the diffraction patterns, all other orientations lie within this segment.

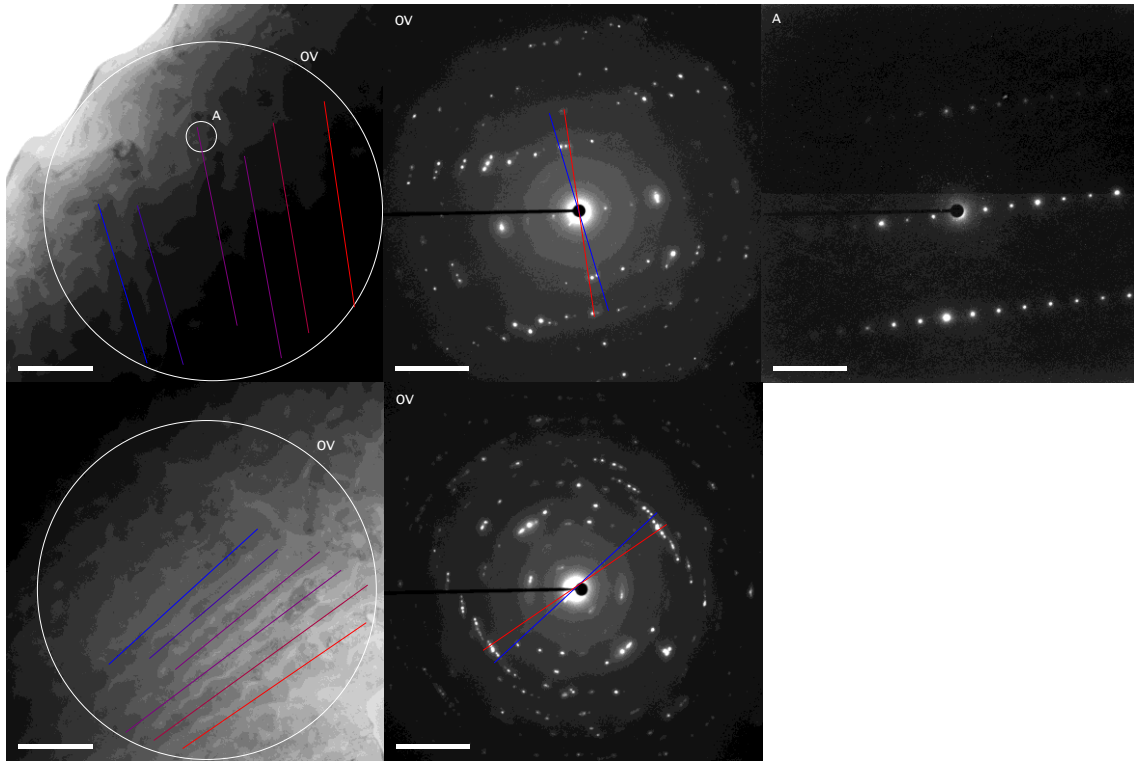


Figure 54: Diffraction done on the lamellae for the 100 K/s heated sample to determine the lamellae directions. The change in angle of the lamellae is indicated by a colour gradient and the two most outlying lines of these segments are shown in the overview diffraction patterns. The $\{-1\ 2\ 0\}$ and $\{-1\ 3\ 0\}$ reflection spots lie within this segment which makes them possible candidates for the growth direction.

The diffraction patterns show spots that lie next to each other within segments similar to the one that is shown. Therefore, it can be concluded that the lamellae have the same growth direction and crystal orientation. All diffraction patterns show the $\{0\ 0\ 1\}$ reflection which is perpendicular to the lamellae orientations. For all diffraction patterns there are two spots that can be found within the segment parallel to the lamellae orientation: the $\{-1\ 2\ 0\}$ and $\{-1\ 3\ 0\}$ reflections (Figure 55). The planar densities of the $\{-1\ 2\ 0\}$ and $\{-1\ 3\ 0\}$ planes are $\frac{3}{ac\sqrt{3}}$ and $\frac{3}{ac\sqrt{7}}$ respectively. Since the planar density of the $\{-1\ 2\ 0\}$ plane is higher, thus it is more likely that this is the growth direction and that the other spots are visible because the lamellae are slightly tilted compared to the viewing direction.

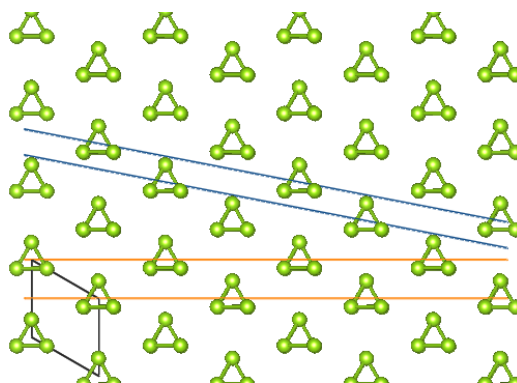


Figure 55: The atomic structure of SeTeAs looking along the $\langle 0\ 0\ 1 \rangle$ axis (left) and a perspective view (right). Two $\{-1\ 2\ 0\}$ planes are shown in orange and two $\{-1\ 3\ 0\}$ planes in blue.

The $\{-1\ 2\ 0\}$ and $\{-1\ 3\ 0\}$ planes are both consistent with the fact that they lie perpendicular to the $\{0\ 0\ 1\}$ planes. The angle between these orientations is 10.9 degrees, thus it should be possible to

rotate from one direction to the other to see which direction is the real growth direction. The lamellae should be longer when viewing perpendicular to the growth direction. Since it turned out to be difficult to rotate the small lamellae while maintaining a Kikuchi pattern, these experiments have not been successful (yet). A last note that has to be made is that it is also possible that the lamellae could be grown like either needles or like plates. However if they would grow like plates, these plates should also be visible on other places in the material when looking in the $\langle 0\ 0\ 1 \rangle$ direction. This was not seen anywhere in the sample. Thus, it is assumed that the lamellae are grown as needles.

4.4.5 Discussion

The melting onset of SeTeAs was not as sharp as SeTe which makes it more difficult to determine the melting temperature. The composition that was inferred from the melting temperature had 40 to 60% tellurium. Since all measurements were done at different heating rates, it is not clear what the influence of the difference in composition was. The 100 K/s heated samples had a difference of 13% in composition. Since there was no large difference found in structure the influence of different compositions is estimated to be small.

The DSC sample was large enough to show multiple spherulites. Since the samples made with the Flash DSC are much smaller and even in the size order of the spherulite size, it is not possible to see these spherulites fully. However, from the lamella orientation and the amorphous boundaries found between lamella that indicate a spherulitic boundary it is assumed that the samples made in the Flash DSC also grow in a spherulitic structure. A question that remains is whether the crystal grow starts randomly within the bulk material or if it starts at the same place like the interface of the sensor. Previous SEM results³³ have shown that in larger samples, there is still crystalline material present at the top of the sample after melt quenching; this could act as seed crystal when the sample is reheated.

The crystals in all samples were found to have the same trigonal structure. The lattice parameters of the crystals did not vary significantly and the change can partly be attributed to the change in composition. Since it was not possible to determine the actual size of the STEM probe, the line scans could not give certainty about the compositional change through the amorphous and crystal material. Even though the amorphous – crystal interface was found to be in the order of a few atoms thick, this does not necessarily hold for the composition change across the interface. Another influence on the lattice parameters could be the amorphous – solid interface. When the nearest neighbour distance is slightly smaller or larger than the crystalline it could induce a strain on the crystal. A larger growth rate contains more lamellae which means the total interfacial area is larger, therefore this effect will be larger.

It was not possible to determine the growth directions of the side chains. The $\{-1\ 2\ 0\}$ and $\{-1\ 3\ 0\}$ planes can go in six directions. However, since the side chains are all found to grow at 90 degree to the main chain it is not possible that the side chains are the same planes as the main chain. Therefore it is more likely that the side chains grow in the $\langle 0\ 0\ 1 \rangle$ direction. In this case only two growth directions are possible. To confirm this, the side chains have to be tilted into a zone axis. However, because of their small size, this is hard to achieve. In addition it has to be noticed that many side chains only grow on one side.

5. Conclusions

The thermal properties such as transition temperatures and enthalpies of SeTeAs and SeTeSb were investigated by the use of DSC. Optical and SEM measurements on SeTeSb showed that Se_3Sb_2 crystals were formed in the ingot which have a melting temperature that is too large to melt in the Flash DSC. These crystals were in the same size order as the Flash DSC samples. Furthermore, the remaining Sb in the other phase was less than 1 at%. In the Flash DSC it was able to switch the material reversibly between the amorphous and crystalline phase. There were however not many differences found compared to SeTe, thus it is assumed that the Se_3Sb_2 and low percentage of Sb did not have much influence on the transition temperatures and enthalpies.

It was also possible to switch SeTeAs reversibly by the use of DSC which showed a different behaviour than SeTe. First of all, the melting peak had a longer onset which was not as sharp as SeTe. Furthermore, at temperatures below 220 °C, the heat capacity was found out to be decreasing during crystallization. It then increased back to the heat capacity of the amorphous state in another transition around 250 – 300 °C. The nature of these transitions could not be fully explained by the DSC measurements. Last, after crystallizing SeTeAs a glass transition could be found which indicates that not all of the material was crystallized while in SeTe this was not observed. Similar to SeTe, the crystallization transition decreased when the percentage of tellurium increased. However, at similar temperatures the crystallization and glass transition peaks lied at higher tellurium percentages than SeTe. Also, the critical quench rate of SeTeAs was found to be much lower than of SeTe, thus by adding arsenic the SeTe it becomes a better glass former. Finally, isothermal measurements at 140 – 160 °C also showed a transition showing up around 200 – 220 °C when the material was reheated after isothermal crystallization.

To find out more about the structural changes that occur when the material is switched reversibly between the crystalline and amorphous phase, a method has been successfully created to measure samples in the SEM and TEM. While in SeTe only one crystalline phase was found, SeTeAs has a more complex two phase structure. The samples that were crystallized by heating them with (ultrafast) DSC showed that the SeTeAs was grown in a spherulitic structure. The spherulites contained crystals that were grown as lamella of which some also contained side chains at 90°. Diffraction patterns taken in the TEM shown that these crystals had a trigonal structure and had a $P3_121$ symmetry which is similar as the crystals in SeTe. Also, by taking diffraction patterns on the lamella it was possible to determine to narrow down the possible growth directions: the $\{-1\ 2\ 0\}$ and $\{-1\ 3\ 0\}$ planes were found. The crystals were surrounded by amorphous phase which is consistent with the glass transition found in the DSC measurements. Furthermore, it was possible to measure the composition of both phases by the use of EDS and STEM. It was found that most of the arsenic (15 – 20 at.%) segregated into the amorphous phase while there was nearly none (0 – 5 at.%) in the crystalline phase. Besides, the crystalline phase contained 20 to 50 at% more tellurium than selenium while the amorphous phase contained 10 to 50 at% more selenium than tellurium. This is consistent with the fact that tellurium is a worse glass former than selenium and arsenic.

There was not much difference found in the structure of a sample of SeTeAs heated at 5 K/s or 100 K/s, thus it is assumed that heating rates in this order of magnitude do not have much influence on the structure. Not all questions that arose from the DSC measurements are answered, the samples that were made in DSC and measured by SEM and TEM provided many details about the structure that could not be measured by DSC or SEM/TEM alone. The method to measure DSC samples in the SEM and TEM offers great opportunities for future research, including answering

these specific questions and investigating the structures of materials at different heating rates and compositions.

6. Outlook

As said in the conclusion, the questions that arose during the DSC measurements were not all answered so far. The transitions that changed the heating rate of SeTeAs at low temperatures were not investigated yet, same for the transition that occurred at high isothermal times during the isothermal measurements. The newly developed method to transfer samples treated by (ultrafast) DSC to the electron microscope can provide an insight in these processes. This can be done by treating samples in the DSC by heating samples either below and above the transition temperature and then transferring them to the electron microscope to see what structural changes occurred during the transition.

Furthermore, more isothermal measurements can be done by varying the time and temperature. So far only a small range of temperatures (140 – 160 °C) has been measured. To prevent evaporation during the measurements, the time of the isothermal segments has to be not too large. Besides that, the influence of the sample size on the transition temperatures in the extended phase diagram and the activation energy is still not fully clear. DSC experiments with different sample sizes combined with microscopy can provide insight on this.

The structure factor calculations that have been done are good to get an idea of how the structure looks. However, since in electron diffraction the behaviour is not kinematical, these calculations are not fully reliable. To obtain a qualitative picture of the structure, structure calculations can be done according to dynamical diffraction theory by using a program such as MacTempas.

So far, several samples were treated with different heating rates to be measured by electron microscopy. However, since both the composition and heating rates at with these samples were treated differed and the structural changes in the samples were small, no clear trends were found. In the future, more samples can be made with different compositions and different heating rates systematically to observe trends. Alongside this, theory about crystal growth can be coupled to the experiments. Although the theory about eutectic growth is well developed³⁹, there is still much to learn for crystal growth in phase change materials¹⁷.

7. Acknowledgements

First of all, I would like to thank Paul Vermeulen, my daily supervisor, who helped me a lot during research and with whom I could also have a nice chat outside of research. Next, I would like to thank Bart Kooi who made it possible for me to do this research and also for teaching me many things during my research. Furthermore, I'd like to thank Gert ten Brink for giving me advice and helping me with my measurements and the various measurement systems I had to use. Finally, I would like to thank the NMI group including the master students for all the nice discussions and talks we had in the coffee breaks.

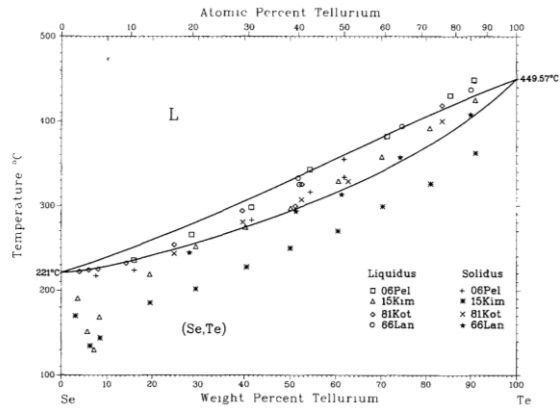
8. References

1. Lencer, D., Salinga, M. & Wuttig, M. Design rules for phase-change materials in data storage applications. *Adv. Mater.* **23**, 2030–2058 (2011).
2. Lencer, D. *et al.* A map for phase-change materials. *Nat. Mater.* **7**, 972–977 (2008).
3. Kolobov, A. V *et al.* Understanding the phase-change mechanism of rewritable optical media. *Nat. Mater.* **3**, 703–708 (2004).
4. Wuttig, M. & Raoux, S. The Science and Technology of Phase Change Materials. *Zeitschrift für Anorg. und Allg. Chemie* **638**, 2455–2465 (2012).
5. Burr, G. W. *et al.* Phase change memory technology. *J. Vac. Sci. Technol. B Microelectron. Nanom. Struct.* **28**, 223 (2010).
6. Wuttig, M. *et al.* Breaking the speed limits of phase-change memory. *Science* **336**, 1566–9 (2012).
7. Sharma, A., Tyagi, V. V., Chen, C. R. & Buddhi, D. Review on thermal energy storage with phase change materials and applications. *Renew. Sustain. Energy Rev.* **13**, 318–345 (2009).
8. Zalba, B., Marín, J. M., Cabeza, L. F. & Mehling, H. *Review on thermal energy storage with phase change: materials, heat transfer analysis and applications. Applied Thermal Engineering* **23**, (2003).
9. Kenisarin, M. & Mahkamov, K. Solar energy storage using phase change materials. *Renew. Sustain. Energy Rev.* **11**, 1913–1965 (2007).
10. Farid, M. M., Khudhair, A. M., Razack, S. A. K. & Al-Hallaj, S. A review on phase change energy storage: Materials and applications. *Energy Convers. Manag.* **45**, 1597–1615 (2004).
11. Wuttig, M. & Yamada, N. Phase-change materials for rewriteable data storage. *Nat. Mater.* **6**, 824–832 (2007).
12. Lo, K. H., Shek, C. H. & Lai, J. K. L. Recent developments in stainless steels. *Mater. Sci. Eng. R Reports* **65**, 39–104 (2009).
13. Speer, J., Matlock, D. K., De Cooman, B. C. & Schroth, J. G. Carbon partitioning into austenite after martensite transformation. *Acta Mater.* **51**, 2611–2622 (2003).
14. Mathot, V. *et al.* The Flash DSC 1, a power compensation twin-type, chip-based fast scanning calorimeter (FSC): First findings on polymers. *Thermochim. Acta* **522**, 36–45 (2011).
15. Orava, J., Greer, A. L., Gholipour, B., Hewak, D. W. & Smith, C. E. Ultra-fast calorimetry study of Ge₂Sb₂Te₅ crystallization between dielectric layers. *Appl. Phys. Lett.* **101**, 91906 (2012).
16. Orava, J., Greer, A. L., Gholipour, B., Hewak, D. W. & Smith, C. E. Characterization of supercooled liquid Ge₂Sb₂Te₅ and its crystallization by ultrafast-heating calorimetry. *Nat. Mater.* **11**, 279–283 (2012).
17. Chen, B., Momand, J., Vermeulen, P. A. & Kooi, B. J. Crystallization Kinetics of Supercooled Liquid Ge-Sb Based on Ultrafast Calorimetry. *Cryst. Growth Des.* **16**, 242–248 (2016).
18. Dhotel, A., Rijal, B., Delbreilh, L., Dargent, E. & Saiter, A. Combining Flash DSC, DSC and broadband dielectric spectroscopy to determine fragility. *J. Therm. Anal. Calorim.* **121**, 453–461 (2015).
19. Oosthoek, J. L. M. *et al.* Correlative transmission electron microscopy and electrical properties study of switchable phase-change random access memory line cells. *J. Appl. Phys.* **117**, 12–17 (2015).
20. Vermeulen, P. a, Momand, J. & Kooi, B. J. Reversible amorphous-crystalline phase changes in a wide range of Se_(1-x)Te_(x) alloys studied using ultrafast differential scanning calorimetry. *J. Chem. Phys.* **141**, 24502 (2014).
21. Shportko, K. *et al.* Resonant bonding in crystalline phase-change materials. *Nat. Mater.* **7**, 653–658 (2008).
22. Debenedetti, P. & Stillinger, F. Supercooled liquids and the glass transition. *Nature* **410**, 259–267 (2001).
23. Angell, C. A. Formation of Glasses from Liquids and Biopolymers Author (s): C . A . Angell Published by : American Association for the Advancement of Science Stable URL :

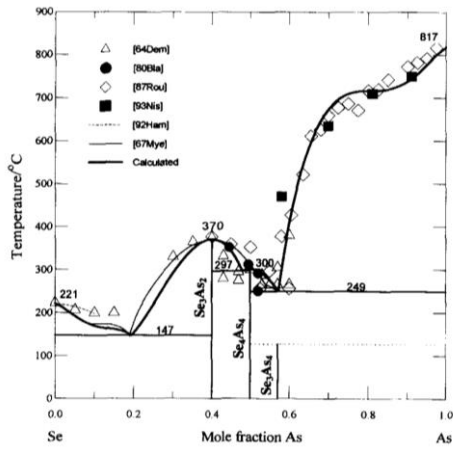
- <http://www.jstor.org/stable/2886440>. *Science* **267**, 1924–1935 (1995).
24. Laidler, K. J. The development of the Arrhenius equation. *J. Chem. Educ.* **61**, 494–498 (1984).
 25. Oosthoek, J. L. M. Structural and electrical characterization of phase-change memory line cells. (University of Groningen, 2014).
 26. Avrami, M. Kinetics of Phase Change. I - General Theory. *J. Chem. Phys.* **7**, 1103 (1939).
 27. Avrami, M. Kinetics of Phase Change. II - Transformation-Time Relations for Random Distribution of Nuclei. *J. Chem. Phys.* **8**, 212–224 (1940).
 28. Avrami, Melvin / (School of Mines, C. U. Kinetics of Phase Change III. Granulation, Phase Change, and Microstructure. *J. Chem. Phys.* **9**, 177–184 (1941).
 29. Keller, R., Holzappel, W. B. & Schulz, H. Effect of pressure on the atom positions in Se and Te. *Phys. Rev. B* **16**, 4404–4412 (1977).
 30. Schiferl, D. & Barrett, C. S. The crystal structure of arsenic at 4.2, 78 and 299°K. *J. Appl. Crystallogr.* **2**, 30–36 (1969).
 31. Barrett, C. S., Cucka, P. & Haefner, K. The crystal structure of antimony at 4.2, 78 and 299°K. *Acta Crystallogr.* **16**, 451–452 (1963).
 32. Wagner, M. *Thermal Analysis in Practice*. (Mettler Toledo, 2009).
 33. Vermeulen, P. a, Momand, J. & Kooi, B. J. Supplementary material for: Reversible amorphous-crystalline phase changes in a wide range of Se_{1-x}Te_x alloys studied using ultrafast differential scanning calorimetry. *J. Chem. Phys.* **141**, 24502 (2014).
 34. Flash DSC-sensor. Available at:
http://www.mt.com/nl/nl/home/products/Laboratory_Analytics_Browse/TA_Family_Browse/ta_accessories_browse/Flash_DSC_Sensor.html. (Accessed: 1st October 2016)
 35. Introduction to electron microscopy. Available at:
http://www.deakin.edu.au/__data/assets/image/0008/272690/introduction.jpg. (Accessed: 1st July 2016)
 36. Turnbull, D. Under what conditions can a glass be formed? *Contemp. Phys.* **10**, 473–488 (1969).
 37. Callister, W. D. *Materials Science and Engineering*. (John Wiley And Sons Ltd, 2010).
 38. Rao, K. J. & Mohan, R. Glass Transitions in As-Se Glasses. *J. Phys. Chem.* **84**, 1917–1919 (1980).
 39. Jackson, K. A. & Hunt, J. D. Lamellar and Rod Eutectic Growth. *Trans. Metall. Soc. AIME* **236**, 1129–1142 (1966).
 40. Gosh, G., Sharma, R. C., Li, D. T. & Chang, Y. A. The Se-Te (Selenium-Tellurium) system. *J. Phase Equilibria* **15**, 213–224 (1994).
 41. Degterov, S. A., Pelton, A. D. & L'Ecuyer, J. D. Thermodynamic optimization of the selenium-arsenic (Se-As) system. *J. Phase Equilibria* **18**, 357–368 (1997).
 42. Eifert, J. R. & Peretti, P. A. The phase diagram of the system tellurium/arsenic. *J. Mater. Sci.* **3**, 293–296 (1968).
 43. Gosh, G. The Sb-Se (antimony-selenium) system. *J. Phase Equilibria* **14**, 753–763 (1993).
 44. Gosh, G. The Sb-Te (antimony-tellurium) system. *J. Phase Equilibria* **15**, 349–360 (1994).

Appendix A: Phase diagrams

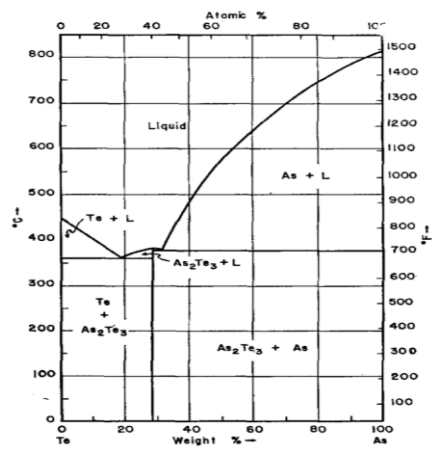
Selenium – Tellurium⁴⁰



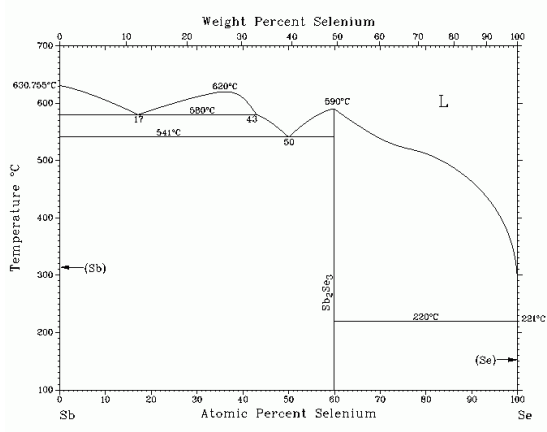
Selenium – Arsenic⁴¹



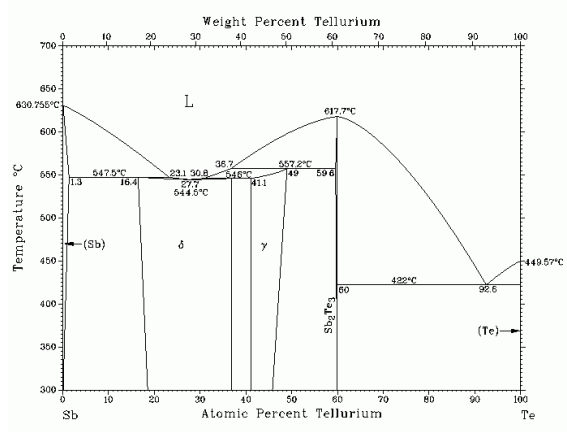
Tellurium – Arsenic⁴²



Selenium – Antimony⁴³



Tellurium – Antimony⁴⁴



Appendix B: Crystallinity and crystal size calculations

The crystallinity and crystal sizes are calculated by the use of the program MATLAB R2015a. First, images with a tif format are loaded into Matlab and a histogram of these images is made. Generally, on optical and SEM images the amorphous material shows up as a dark contrast and the crystalline material as a bright contrast. In the histogram, this shows up as two peaks. A threshold is done in the middle of these two peaks which sets everything below the threshold to 0 (amorphous) and everything above the threshold to 1 (crystalline) (Figure 56).

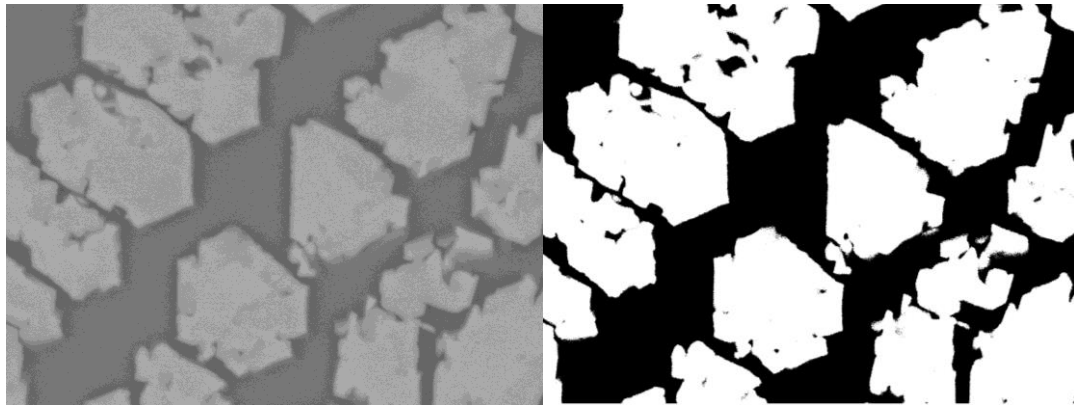


Figure 56: A SEM image of SeTeAs crystals surrounded by amorphous material (left) and the threshold image of it (right). The bright and white areas are the crystals and the dark and black areas are the amorphous material.

The crystallinity is then calculated by adding all white pixels and dividing it by the total amount of pixels. To find an average of the crystal size, the amount of crystals in the picture has to be determined. For this, the Matlab algorithm `bwconncomp` is used on the threshold image (Figure 57). This function acts on a binary image and groups pixels with a binary value of 1 (thus above the threshold) that are connected to each other.

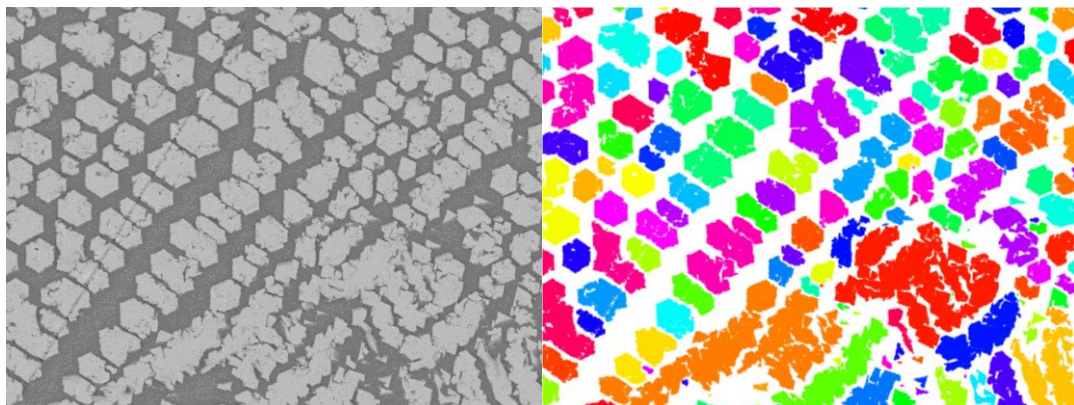


Figure 57: A SEM image of SeTeAs crystals surrounded by amorphous material (left) and an image where the individual crystals are colored (right). The amorphous material in the colored image shows up as white.

As can be seen in the figure, some crystals have grown together and are counted as one while there are also some crystal areas present that are much smaller. Since it is sometimes difficult to distinguish if two crystals are grown together or if they should still be treated as separate, this method still gives a good indication of the amount of crystals in the image. Of course, more crystals in an image give better statistics, but it also lowers the amount of pixels per crystal or amorphous material between the crystals which can make it more difficult to distinguish separate crystals.

Appendix C: Structure factor of the trigonal system and P 3₁ 2 1 space group

To determine the structure factor for trigonal system with a P 3₁ 2 1 space group, the positions of the atoms in the primitive cell are required. For this structure there are three atoms which have a certain distance α from the rotation axis as shown in Table 11.

Atom	x	y	z
1	$-\alpha$	$-\alpha$	0
2	α	0	$1/3$
3	0	α	$2/3$

Table 11: The atomic positions within the trigonal unit cell for the P 3₁ 2 1 symmetry group. The parameter α determines the distance from the atoms to the rotation axis.

The structure factor can then be determined as follows:

$$F = \sum_i f_i e^{i\mathbf{g} \cdot \mathbf{r}_i}$$

$$F = f_1 e^{2\pi i(-ah-\alpha k)} + f_2 e^{2\pi i(ah+\frac{1}{3}l)} + f_3 e^{2\pi i(\alpha k+\frac{2}{3}l)}$$

For $l = 3n$ and $h, k = 0$, this equation gives:

$$F = f_1 e^{0\pi i n} + f_2 e^{2\pi i n} + f_3 e^{4\pi i n}$$

$$F = f_1 + f_2 + f_3$$

Thus the $\{0\ 0\ 3n\}$ peaks give constructive interference. For $l = 3n + 1$ and $h, k = 0$ the equation becomes:

$$F = f_1 e^{0\pi i n} + f_2 e^{2\pi i n} e^{\frac{2}{3}\pi i} + f_3 e^{4\pi i n} e^{\frac{4}{3}\pi i}$$

$$F = f_1 + f_2 \left(-\frac{1}{2} + i\frac{\sqrt{3}}{2} \right) + f_3 \left(-\frac{1}{2} - i\frac{\sqrt{3}}{2} \right)$$

$$F = f_1 - \frac{1}{2}(f_2 + f_3) + i\frac{\sqrt{3}}{2}(f_2 - f_3)$$

The same can be done for $l = 3n + 2$ and $h, k = 0$:

$$F = f_1 e^{0\pi i n} + f_2 e^{2\pi i n} e^{\frac{4}{3}\pi i} + f_3 e^{4\pi i n} e^{\frac{8}{3}\pi i}$$

$$F = f_1 + f_2 \left(-\frac{1}{2} - i\frac{\sqrt{3}}{2} \right) + f_3 \left(-\frac{1}{2} + i\frac{\sqrt{3}}{2} \right)$$

$$F = f_1 - \frac{1}{2}(f_2 + f_3) + i\frac{\sqrt{3}}{2}(f_3 - f_2)$$

When all atomic form factors are the same, these last two conditions give a structure factor of 0 which means there is destructive interference. Thus for pure Se or Te the $\{0\ 0\ 2n+1\}$ and $\{0\ 0\ 2n+2\}$ reflections are not visible. However as said, for SeTeAs the atomic form factors are different thus the $\{0\ 0\ 2n+1\}$ and $\{0\ 0\ 2n+2\}$ reflections will not be nonzero.

Appendix D: Composition data of SeTeAs

The data of all compositional measurements done with TEM-EDS are listed below in tables. Included is the average and standard deviation of each measurement, which is used in the graphs of this thesis.

Ingot

	Measurement	As (at%)	Se (at%)	Te (at%)
Amorphous	1	21.4	62.6	16.0
	2	20.3	62.1	17.5
	3	21.2	62.7	16.0
	Average	21.0±0.6	62.5±0.3	16.5±0.9
Crystalline	1	0.0	41.6	58.4
	2	0.1	37.8	62.1
	3	0.3	37.8	61.9
	Average	0.1±0.2	39.1±2.2	60.8±2.1

5 K/s heated sample

	Measurement	As (at%)	Se (at%)	Te (at%)
Overview	1	6.7	39.4	53.9
	2	7.3	41.3	51.4
	3	7.3	40.4	52.3
	4	7.2	39.8	53
	Average	7.1±0.3	40.2±0.8	52.7±1.1
Amorphous	1	14.7	48.8	36.5
Crystalline	1	5.0	37.0	58.0

100 K/s (1) heated sample

	Measurement	As (at%)	Se (at%)	Te (at%)
Overview	1	12.0	41.6	46.4
	2	5.7	56.4	37.8
	3	10.1	35.6	54.3
	4	7.9	39.0	53.1
	5	9.4	34.2	56.4
	Average	9.0±2.4	41.4±8.9	49.6±7.6

100 K/s (2) heated sample

	Measurement	As (at%)	Se (at%)	Te (at%)
Overview	1	10.3	40.2	49.5
	2	11.3	42.5	46.2
	3	11.3	44.4	44.4
	4	9.7	36.4	53.9
	Average	10.7±0.8	40.9±3.4	48.5±4.2
Amorphous	1	21.1	49.5	29.4
Crystalline	1	2.1	23.1	74.7

-100 K/s heated sample

	Measurement	As (at%)	Se (at%)	Te (at%)
Overview	1	6.5	39.9	53.6
	2	7.9	41.2	50.9
	3	5.9	40.4	53.7
	Average	6.8±1.0	40.5±0.7	52.7±1.6
Amorphous	1	18.7	56.8	24.5
	2	21.3	57.7	21.0
	3	19.8	58.8	21.4
	4	18.9	59.6	21.5
	5	19.3	58.2	22.5
	6	19.7	58.9	21.4
	Average	19.6±0.9	58.3±1.0	22.1±1.3
Crystalline	1	3.0	34.5	62.5
	2	5.8	40.4	53.8
	3	3.8	35.1	61.1
	4	2.8	33.3	63.9
	5	1.6	34.3	64.1
	Average	3.4±3.5	35.5±2.8	61.1±4.2